

University of Central Florida

STARS

Graduate Thesis and Dissertation 2023-2024

2023

Laser Powder Bed Fusion of Bimetallic Structures

Asif Mahmud

University of Central Florida



Part of the [Metallurgy Commons](#)

Find similar works at: <https://stars.library.ucf.edu/etd2023>

University of Central Florida Libraries <http://library.ucf.edu>

This Doctoral Dissertation (Open Access) is brought to you for free and open access by STARS. It has been accepted for inclusion in Graduate Thesis and Dissertation 2023-2024 by an authorized administrator of STARS. For more information, please contact STARS@ucf.edu.

STARS Citation

Mahmud, Asif, "Laser Powder Bed Fusion of Bimetallic Structures" (2023). *Graduate Thesis and Dissertation 2023-2024*. 30.

<https://stars.library.ucf.edu/etd2023/30>

LASER POWDER BED FUSION OF BIMETALLIC STRUCTURES

by

ASIF MAHMUD

M.S. University of Central Florida, 2020

B.S. Bangladesh University of Engineering and Technology, 2017

A dissertation submitted in partial fulfillment of the requirements
for the degree of Doctor of Philosophy
in the Department of Materials Science and Engineering
in the College of Engineering and Computer Science
at the University of Central Florida
Orlando, Florida.

Fall Term
2023

Major Professor: Yongho Sohn

© 2023 Asif Mahmud

ABSTRACT

Laser powder bed fusion (LPBF) is a popular additive manufacturing (AM) technique that has demonstrated the capability to produce sophisticated engineering components. This work reports the crack-free fabrication of an SS316L/IN718 bimetallic structure via LPBF, along with compositional redistribution, phase transformations and microstructural development, and nanohardness variations. Constituent intermixing after LPBF was quantitatively estimated using thermo-kinetic coefficients of mass transport and compared with the diffusivity of Ni in the austenitic Fe-Ni system. The intermixing of primary solvents (Ni and Fe) in SS316L/IN718 bimetallic structures was observed for an intermixing zone of approximately 800 μm , and their intermixing coefficient was estimated to be in the order of $10^{-5} \text{ m}^2/\text{s}$ based on time of 10 ms. In addition, to understand the high temperature behavior, SS316L/IN718 bimetallic structures were annealed at 850, 950, and 1050 $^{\circ}\text{C}$, for 120, 48, and 24h respectively, followed by water quenching (WQ). Furthermore, to better understand the intermixing of individual components (Ni and Fe) and to predict the varying (maximum) temperatures in LPBF of SS316L/IN718 bimetallic structures, solid-to-solid SS316L vs IN718 diffusion couples were examined at 850, 950, and 1050 $^{\circ}\text{C}$, for 120, 48, and 24h respectively, followed by WQ. The investigation of SS316L vs IN718 diffusion couples yielded a maximum temperature of approximately 3400 K in the LPBF of SS316L/IN718 bimetallic structures. Finally, compositional redistribution, phase transformations and microstructural development, and nanohardness variations after LPBF of SS316L/IN625 bimetallic structure were also investigated to provide a better understanding of the LPBF process via bimetallic fabrication.

Keywords: Constituent intermixing, bimetallic structure, laser powder bed fusion, diffusion couple, nanohardness.

ACKNOWLEDGEMENTS

First and foremost, I would like to take the opportunity to thank my parents, spouse, family members and friends for their spiritual support throughout the journey and for always being there whenever I needed them the most.

I would like to thank my advisor Dr. Yongho Sohn for giving me the opportunity to pursue research of my interest, use of his facilities, and his continual support. I would also like to thank my dissertation committee members Dr. Akihiro Kushima, Dr. Tengfei Jiang, Dr. Kristopher Davis, Dr. Yuanli Bai for agreeing to serve on my committee as well as provide feedback and support for this work.

A special shout-out to my colleagues at Laboratory for Advanced Materials and Additive Manufacturing for their help wherever needed. The use of instruments at the Materials Characterization facility (MCF) of University of Central Florida was important in this work and I would like to acknowledge Ms. Sandra Griggs, Mr. Kirk Scammon, and Mr. Mikhail Klimov for their assistance.

TABLE OF CONTENTS

| | |
|---|-----|
| LIST OF FIGURES | vii |
| LIST OF TABLES | x |
| LIST OF ACRONYMS | xi |
| CHAPTER 1: INTRODUCTION | 1 |
| CHAPTER 2: LITERATURE REVIEW | 3 |
| 2.1 Processing with Additive Manufacturing | 3 |
| 2.2 Metallurgy & Applications of SS316L, IN718, and IN625 Alloys | 3 |
| 2.3 Additive Manufacturing of Functionally Graded Materials (FGM) and Bimetallic Structures | 5 |
| 2.4 Literature on Interdiffusion Coefficients of Ni | 9 |
| 2.5 Purpose of this Doctoral Dissertation | 14 |
| CHAPTER 3: METHODOLOGY | 15 |
| 3.1 LPBF of SS316L/IN718 Bimetallic Structure | 15 |
| 3.2 SS316L vs IN718 Diffusion Couples from SS316L/IN718 Bimetallic Structure | 17 |
| 3.3 Heat Treatment of SS316L/IN718 Bimetallic Structure | 18 |
| 3.4 LPBF of SS316L/IN625 Bimetallic Structure | 19 |
| 3.5 Phase Constituents and Microstructure Analysis | 21 |
| 3.6 Mechanical Properties via Nanohardness Test | 21 |
| CHAPTER 4: RESULTS AND DISCUSSIONS | 23 |

| | |
|---|----|
| 4.1 LPBF of SS316L/IN718 Bimetallic Structure | 23 |
| 4.1.1 Phase Constituents and Microstructure:..... | 23 |
| 4.1.2 Constituent Intermixing and Nanohardness..... | 26 |
| 4.2 Heat Treatment of SS316L/IN718 Bimetallic Structures Fabricated by LPBF..... | 30 |
| 4.3 SS316L vs IN718 Diffusion Couples from SS316L/IN718 Bimetallic Structures | 37 |
| 4.4 LPBF of SS316L/IN625 Bimetallic Structure | 45 |
| 4.4.1 Phase Constituents and Microstructure:..... | 45 |
| 4.4.2 Constituents Intermixing and Nanohardness: | 49 |
| CHAPTER 5: SUMMARY..... | 51 |
| APPENDIX: PUBLICATIONS AND CONFERENCES..... | 53 |
| List of Publications | 54 |
| List of Conferences..... | 55 |
| LIST OF REFERENCES | 56 |

LIST OF FIGURES

| | |
|---|----|
| Figure 1: Secondary electron (SE) micrographs of virgin (a) SS316L and (b) IN718 powders .. | 16 |
| Figure 2: (a) A schematic of the layer-by-layer fashion of fabrication of bimetallic structures via LPBF. A slice thickness of 30 μm was used to build both SS316 and IN718 to 6 mm in height; (b) Fabricated SS316L/IN718 bimetallic structures. The diameter and height of the cylinders were 10 mm and 12 mm, respectively. | 17 |
| Figure 3: Secondary electron micrographs of virgin (a) SS316L and (b) IN625 powders. | 19 |
| Figure 4: Fabricated SS316L/IN625 bimetallic structures. The diameter and height of the cylinders were 10 mm and 12 mm, respectively. | 20 |
| Figure 5: X-ray diffraction patterns of SS316L_XY, IN718_XY, and SS316L/IN718 interface region_XZ cross sections collected from fabricated SS316L/IN718 bimetallic structure. | 24 |
| Figure 6: Optical Micrographs of SS316L/IN718 interface cross section: (a) unetched, (b) low magnification etched and (c) high magnification etched. | 25 |
| Figure 7: Electron micrographs of SS316L/IN718 bimetallic interface cross section: (a) low magnification BSE micrographs revealing the entire cross section, (b) backscattered electron micrographs revealing the cellular/columnar microstructure of the interface, (c) high magnification micrographs revealing the cellular/columnar microstructure along with the carbides and laves phases. | 26 |
| Figure 8: Concentration profiles of Fe, Ni and Cr, and (b) Nanohardness profile in the vicinity of SS316L/IN718 bimetallic interface. | 27 |
| Figure 9: Intermixing coefficient of Ni and Fe as a function of time in SS316L/IN718 bimetallic structures: (a) Time in ms, (b) Time in s | 30 |

Figure 10: Concentration profiles of Fe, Ni, and Cr in the vicinity of SS316L/IN718 bimetallic interface before and after annealing: (a) As fabricated, (b) 850 °C for 120h, (c) 950 °C for 48h, and (d) 1050 °C for 24h followed by WQ. 31

Figure 11: Concentration profiles of Fe and Ni expressed in terms of relative concentration in the vicinity of annealed SS316L/IN718 bimetallic interface: (a) As-fabricated, (b) 850 °C for 120h, (c) 950 °C for 48h, and (d) 1050 °C for 24h followed by WQ. 32

Figure 12: Etched optical micrographs of SS316L/IN718 bimetallic interface cross section before and after annealing: (a) As-fabricated, (b) 850 °C for 120h, (c) 950 °C for 48h, and (d) 1050 °C for 24h followed by WQ. 34

Figure 13: Electron micrographs demonstrating the change in microstructure before and after annealing of SS316L/IN718 bimetallic structure: (a, b) As-fabricated, (c, d) 850 °C for 120h, (e, f) 950 °C for 48h, and (g, h) 1050 °C for 24h followed by WQ. 35

Figure 14: Nanohardness of SS316L, SS316L/IN718 bimetallic interface region, and IN718 before and after annealing. 36

Figure 15: Unetched optical micrographs of the interface microstructure of SS316L vs IN718 diffusion couples annealed at (a) 850 °C for 120h, (b) 950 °C for 48h, and (c) 1050 °C for 24h followed by WQ. 38

Figure 16: Concentration profile and corresponding interdiffusion fluxes of Ni and Fe from SS316L vs IN718 diffusion couples annealed at (a) (a) 850 °C for 120h, (b) 950 °C for 48h, and (c) 1050 °C for 24h followed by WQ. 38

Figure 17: Etched optical micrographs of the interface microstructure of SS316L vs IN718 diffusion couples annealed at (a) 850 °C for 120h, (b) 950 °C for 48h, and (c) 1050 °C for 24h followed by WQ. 39

Figure 18: Temperature dependence of average effective interdiffusion coefficients for (a) Ni, and (b) Fe determined from SS316L vs IN718 diffusion couples in the temperature range from 850 to 1050 °C. 40

Figure 19: Temperature dependence of Ni self-diffusion coefficients in the temperature range of 1520 to 1945 K. This plot was done using Meyer’s Ni self-diffusion coefficients data. 44

Figure 20: X-ray diffraction patterns of SS316L_XY, IN625_XY, and SS316L/IN625 interface cross sections collected from fabricated SS316L/IN625 bimetallic structure. 46

Figure 21: Optical Micrographs of SS316L/IN625 interface cross section: (a) unetched, (b) etched. 47

Figure 22: Electron micrographs of SS316L/IN625 bimetallic interface cross section: (a) low magnification BSE micrographs revealing the entire cross section, (b) BSE micrographs revealing the overlapping of the melt pools (c) high magnification SE micrographs revealing the cellular/columnar microstructure, and (d) high magnification SE micrographs revealing potential laves phases. 48

Figure 23: (a) Concentration profiles of Fe, Ni and Cr; (b) nanohardness profile in the vicinity of SS316L/IN625 bimetallic interface. 49

Figure 24: Intermixing coefficient of Ni and Fe as a function of time in SS316L/IN625 bimetallic structures: (a) Time in ms. (b) Time in s 50

LIST OF TABLES

| | |
|--|----|
| Table 1: Chemical composition in wt% of SS316L powders [33] | 5 |
| Table 2: Chemical composition in wt% of IN718 powders [34] | 5 |
| Table 3: Chemical composition in wt% of IN625 powders [35] | 5 |
| Table 4: Low Temperature Diffusivity of Ni in the Fe-Ni system [44]..... | 9 |
| Table 5: Diffusion Coefficient of Ni in the Fe-Ni Diffusion Couples [45] | 10 |
| Table 6: Values of D_0 and Q in Binary Fe-Ni Austenite [45] | 10 |
| Table 7: Concentration Dependence of Diffusion Coefficients of Ni in Fe-Ni system [46]. | 11 |
| Table 8: Self-diffusion coefficients of Ni determined by quasi neutron elastic scattering [50]. .. | 13 |
| Table 9: Chemical Composition (wt. %) of SS316L powders determined by XEDS. | 15 |
| Table 10: Chemical Composition (wt. %) of IN718 powders determined by XEDS. | 15 |
| Table 11: Diffusion coefficient of Ni in Fe-Ni diffusion couples and intermixing coefficient estimated in SS316L/IN718 bimetallic structure produced by LPBF. | 30 |
| Table 12: Average effective interdiffusion coefficients and the corresponding Activation Energy and Pre-exponential factor of Ni and Fe determined from SS316L vs IN718 diffusion couple. . | 40 |
| Table 13: Activation energy (Q) and Pre-exponential constant (D_0) extracted from relevant literatures and this study. | 41 |
| Table 14: Diffusion coefficient of Ni in Fe-Ni and SS316L vs IN718 diffusion couples and intermixing coefficient estimated in SS316L/IN718 bimetallic structures produced via LPBF. . | 42 |
| Table 15: Extrapolation of Meyer et al. [50] self-diffusion coefficients of Ni to 3400 K..... | 44 |

LIST OF ACRONYMS

| | |
|------|---|
| AM | Additive Manufacturing |
| BAMS | Bimetallic Additively Manufactured Structures |
| BSE | Back Scattered Electron |
| CAD | Computer Aided Design |
| DED | Directed Energy Deposition |
| EBM | Electron Beam Melting |
| FGM | Functionally Graded Materials |
| HCP | Hexagonal Close Packed |
| HT | Heat Treatment |
| GMAW | Gas-Metal-Arc-Welding |
| LENS | Laser Engineered Net Shaping |
| LPBF | Laser Powder Bed Fusion |
| OEM | Original Equipment Manufacturer |
| SE | Secondary Electron |
| SEM | Scanning Electron Microscope |
| UTS | Ultimate Tensile Strength |
| VED | Volumetric Energy Density |
| WAAM | Wire-Arc Additive Manufacturing |
| XRD | X-ray Diffraction |

CHAPTER 1: INTRODUCTION

Additive manufacturing (AM), commonly known as three-dimensional (3D) printing, typically refers to a process in which an engineering component is built in a layer-by-layer fashion close to their final (net) shape. This net-shape capability of manufacturing sophisticated parts with a high degree of accuracy from a computer aided design (CAD) model and the potential for powder reuse, reduced cost and manufacturing steps make the AM a promising technology [1–3]. Laser powder bed fusion (LPBF) is a popular AM technique that can produce dense, complex parts by selectively melting the powder bed with a laser source in a layer-by-layer process [4–7]. Furthermore, stopping and restarting the process in LPBF has been observed to have minimal effects on the microstructure and indentation-based mechanical properties of certain alloys [8]. This advantage of LPBF can be utilized to fabricate bimetallic structures (a structure consisting of two dissimilar metals and alloys).

In the past, the joining of two metals/alloys was achieved through a variety of joining techniques, such as welding, brazing, or soldering. However, the metallurgical characteristics of traditional welding processes can result in an increased number of precipitates and intermetallics and the distortion of the weld interface, all of which are detrimental to the structural integrity of the final components. AM presents a viable alternative; it has the potential to avoid the complications found in traditional welding process and, most importantly, allows for the joining of metals/alloys without the use of any filler material [9].

Extreme environment applications such as in gas turbine engines, aerospace applications, or nuclear power generation require engineering components that must work at entirely different temperatures and at different locations or require site-specific properties throughout the component [10]. However, it can be challenging to leverage such characteristics from a single material, and

this warrants the development of structural components with tailored properties. A bimetallic structure combines dissimilar alloys/metals with different density, thermal and mechanical properties, and has the potential to provide a solution to this challenging dilemma. To reduce the deadweight in automobiles, bimetallic materials have been suggested for use in the creation of body frames, engines, and pistons [11,12]. The applications of bimetallic structures range from reactors to heat exchangers in chemical industries, where some parts are required to be high-corrosion and high-temperature-resistant (e.g., IN625 or IN718) while other parts are required to have good mechanical endurance/ductility (e.g., SS316L) [13]. These two alloys could provide promising opportunities in dissimilar material structures [14].

CHAPTER 2: LITERATURE REVIEW

2.1 Processing with Additive Manufacturing

Additive manufacturing (AM) is an emerging field in which an engineering component is built using a computer aided design (CAD) in a layer-by-layer fashion [15,16]. The typical working procedure for AM involves the incremental deposition of material, typically in powdered form, one layer at a time. This is accomplished via commonly used technology like powder bed fusion (PBF) or directed energy deposition (DED). The PBF process can further be classified based on the heating source used. The heating sources can either be laser or electron beam. PBF and DED typically differ on how the powder is fed into the melt pool. In DED, powders are deposited where desired using a nozzle attached with a laser. In PBF, the powder is spread into a thin layer (i.e., powder bed) over the build plate and selectively melted by a laser source and ultimately build a 3D part layer by layer [17]. LPBF is typically performed at 1 atm in an inert atmosphere (Ar or N₂). Flowing Ar or N₂ during LPBF does not guarantee a complete vacuum, however, it minimizes the O₂ content significantly.

Typically, in LPBF, there are four main processing parameters: laser power, laser scan speed, distance between consecutive scans known as hatch spacing, and the thickness of each powder bed layer, referred to as slice thickness. These four terms can be normalized into volumetric energy density (VED) and defined by equation 1 [18–22]:

$$VED = \frac{\text{Laser Power}}{\text{Laser Scan Speed} \times \text{Hatch Spacing} \times \text{Slice Thickness}} \quad \text{J/mm}^3 \quad (1)$$

2.2 Metallurgy & Applications of SS316L, IN718, and IN625 Alloys

The 316L stainless steel is a member of the austenitic steels with chromium-nickel-molybdenum alloying additions and has a carbon content lower than 0.03 wt%. The SS316L has

good weldability, machinability, mechanical properties and in combination with superior corrosion resistance it has a wide range of applications. The notable applications include nuclear reactors [23], metallic biomaterial [24], fuel cells [25] and marine applications [26].

Inconel 718, often abbreviated as IN718, is an age-hardenable Ni-Cr-Fe based superalloy and has been used in the aeronautics and energy industries due to its ability to retain mechanical stability up to 650 °C, excellent oxidation resistance, and good fatigue life [3]. In addition, IN718 is widely used to manufacture exhaust pipes, parts for rocket motors, gas turbines, and nuclear reactors [27]. IN718 is typically precipitation hardened by the γ' -Ni₃(Al, Ti) with L1₂ crystal structure and γ'' -Ni₃Nb with DO₂₂ crystal structure. Typically, as-built PBF IN718 alloy consists of fine cellular or columnar dendritic microstructure resulting from the rapid cooling rate. Nb, Mo and Ti were segregated along the cellular boundary and interdendritic region and formed nanoscale Laves and carbides. Precipitates of γ' or γ'' were not observed in the as-built IN718 alloy [3]. The formation of the Laves phase occurs through the eutectic reaction $L \rightarrow \gamma + \text{Laves}$ and is typically enriched with Nb [28].

Inconel 625 (IN625) is a solid-solution strengthened, nickel-chromium super alloy containing significant amount of iron, niobium and molybdenum and has excellent weldability, creep resistance, and corrosion resistance as well as high yield, creep, fatigue, and tensile strength [29]. In addition, it has widespread applications in aeronautic, aerospace, marine, chemical, and petrochemical industries and also being used for reactor-core and control-rod components in pressurized water reactors and as heat exchanger tubes [30]. However, segregation of solute elements during solidification in the welding process results in the precipitation of secondary phases such as γ'' , δ , Laves phases, and carbides. Similar phase evolution was also reported in rapidly solidified IN625 alloy [31,32].

The nominal composition in wt% of SS316L, IN718 and IN625 powders obtained from the original equipment manufacturer (OEM, SLM Solutions) are reported in Table 1, Table 2, and Table 3, respectively.

Table 1: Chemical composition in wt% of SS316L powders [33]

| Fe | Cr | Ni | Mo | Nb+Ta | Mn | Si | P | S | C | N | O |
|------|-------|-------|-------|-------|-----|-----|-------|------|------|------|---|
| Bal. | 16-18 | 10-14 | 2-3.0 | - | 2.0 | 1.0 | 0.045 | 0.03 | 0.03 | 0.10 | - |

Table 2: Chemical composition in wt% of IN718 powders [34]

| Ni | Cr | Fe | Mo | Nb | Ti | Al | Si | Mn |
|-----------|-----------|-------|-----------|-----------|-----------|-----------|------|------|
| 50.0-55.0 | 17.0-21.0 | Bal. | 2.80-3.30 | 4.75-5.50 | 0.65-1.15 | 0.20-2.80 | 0.35 | 0.35 |
| Co | P | S | B | Cu | C | | | |
| 1.0 | 0.015 | 0.015 | 0.006 | 0.30 | 0.08 | | | |

Table 3: Chemical composition in wt% of IN625 powders [35]

| Ni | Cr | Mo | Nb | Fe | Co | Si | Mn | Ti | Al | C | S | P |
|------|-------|------|-----------|------|-----|------|------|------|------|------|-------|-------|
| Bal. | 20-23 | 8-10 | 3.15-4.15 | 5.00 | 1.0 | 0.50 | 0.50 | 0.40 | 0.40 | 0.10 | 0.015 | 0.015 |

2.3 Additive Manufacturing of Functionally Graded Materials (FGM) and Bimetallic Structures

In advanced engineering applications, especially in extreme environments, there's a demand for engineering parts that exhibit varying properties depending on their precise location within the component. It is often challenging to get such varying characteristics from a single

material. This calls for the use of FGM or bimetallic structures which in general is defined as joining of two dissimilar materials with gradients (zero gradients for bimetallic) in structure or composition. Thus, FGM has the capability of creating a combination of various advanced properties that are theoretically impossible to be simultaneously possessed by a single material [12,36]. Hinojos *et al.* [9] reported the fabrication of IN718 onto 316L stainless steel substrate and SS316L onto Inconel substrate via electron beam melting (EBM) and reported cracking at the interface of SS316L deposited onto Inconel substrate. Locci *et al.* [37] studied the diffusion bonding and brazing of SS316L and IN718 for heat exchanger applications which required survival for prolonged time at around 560 °C. Hot press diffusion bonding revealed sound bonding with/without a pure nickel interlayer, however, fine porosity was observed at the interfaces, and could be reduced with higher pressures and optimized bonding parameters. For the brazing process, nickel based brazes and gold based brazes were used. Gold based brazes (Nicro) were recommended for brazing of SS316L and IN718 for heat exchanger application based on minimum chemical interaction and lowest impact on the base metal strength. Click or tap here to enter text. Click or tap here to enter text. Singh *et al.* [13] reported the fabrication of crack free bimetallic SS316L on top of IN718 structure via LPBF and observed good interface bonding. They reported an ultimate tensile strength (UTS) of 547.8 MPa and ductility of 21.2% for IN718/SS316L bimetallic structure. Ghanavati *et al.* [28] reported the fabrication of thin walled IN718 on top of SS316L FGM via directed energy deposition. This study included fabrication of 3 thin walled FGM (3 layers of IN718 on top of 3 layers of SS316L). Sample 1 was fabricated with no gradient transition between 3 layers of SS316L and 3 layers IN718, sample 2 consisted of 2 layers with an equal weight percentage of base alloys sandwiched between 2 layers of SS316L from the bottom and 2 layers of IN718 from the top. Sample 3 started with 100 wt% SS316L from the bottom

followed by a decrease of 20 wt% of SS316L in each subsequent step to form 100 wt% IN718 in the topmost layer. No defect was observed in sample 1 while sample 3 reported highest defects owing to significant amount of powder mixture in different proportions and different thermal behavior of the base alloys. In another work, Ghanavati et al. [38] reported fabrication of SS316L/IN718 FGM via LPBF. Three samples were fabricated: F0-Bimetallic (100 wt % IN718 and 100 wt % SS316L), F50 (100 wt % IN718, 50-50 wt % IN718 and SS316L, and 100 wt % SS316L) and F25 (100 wt % IN718, 25-75 wt % SS316L and IN718, 50-50 wt % IN718 and SS316L, and 75-25 wt % SS316L and IN718, and 100 wt % SS316L). The ratios of powders wt % 75- 25, 50-50 and 25-75 were prepared by automatic mechanical mixing uniformly inside separate containers for an hour. The EBSD results of the bimetallic sample (F0) indicated an epitaxial growth in the transition zone due to same crystal structure, anisotropic orientation, increase in grain size and decrease in density of high angle grain boundaries due to decrease in temperature gradient and cooling rate. The tensile result showed the gradient design with a 50 wt% mixed intermediate zone exhibited a tensile strength of 610 MPa and elongation of 31.5 % while the F25 sample exhibited significantly lower toughness and ductility in indicating a premature failure from the 25 wt% IN718 zone. The F0 bimetallic SS316L/IN718 showed a tensile strength of 581.72 MPa and ductility of 33.5 %. Mei et al. [39] investigated the fabrication of SS316L/IN718/SS316L sandwich structure via LPBF and reported elasticity modulus of 103 ± 3 MPa, ductility of $28.1 \pm 2\%$ and UTS of 596 ± 10 MPa indicating good metallurgical bonding at the interfaces (reported interface width was approximately 100 μm) between 316SS and IN718 structure. However, some cracks were found at or near the interface.

Kim et al. [40] reported the fabrication of crack free bimetallic additively manufactured structure (BAMS) IN625 on top of SS316L manufactured by a gas-metal-arc-welding (GMAW)

based on wire-arc additive manufacturing (WAAM) technology and investigated the influence of heat treatment on the microstructure and mechanical properties. Chen et al. [14] reported the microstructural evolution and crack formation in additively manufactured SS316L and IN625 bimetallic structure via DED technique by alternating the printing sequence. Two types of interfaces (Type 1: IN625 deposition on top of SS316L; Type 2: SS316L deposition on top of IN625) were generated by changing the printing sequence. They observed high cracking susceptibility in Type 2 interface which was attributed to solidification and liquidation cracking. Feenstra et al. [41] investigated the influence of varying volumetric energy density (VED) on the interface and mechanical properties of SS316L deposited onto IN625 fabricated on mild steel substrate via DED. The yield strength and UTS were observed to be higher compared to wrought SS316L. However, significantly lower ductility was reported. The compositional transitional zone revealed the formation of γ' -Ni₃Nb precipitates enriched with Mo. Ahsan et al. [42] reported the fabrication of IN625 on top of SS316L BAMS via GMAW + WAAM system. Mechanical testing yielded UTS of 600 MPa and ductility of 40 %, with the failure location on the stainless-steel side. In addition, no defects or intermetallic were observed at the interface region. Ahsan et al. [43] also reported the influence of heat treatment on SS316L deposited on top of low carbon steel BAMS via GMAW + WAAM system. Heat-treatment at 950 °C for 1h resulted in 35% and 250% increases in the UTS and ductility, compared to the as-built BAMS. Carroll et al. [10] reported fabrication of IN625 on top of SS304L FGM via DED and studied the microstructure, phase composition and microhardness. Cracks were reported near the SS304 end of the gradient zone due to formation of a secondary phase.

Current literature primarily emphasizes aspects related to the design and fabrication, microstructure, and mechanical properties of FGM and bimetallic structures. To the best of the

author's knowledge, there has been a noticeable absence of studies focusing on the intermixing of the constituent elements within the bimetallic structures. This doctoral dissertation focusses on addressing this research gap by placing particular emphasis on the intermixing of constituent elements in the context of SS316L/IN718 bimetallic fabrication.

2.4 Literature on Interdiffusion Coefficients of Ni

Narayan *et al.* [44] reported a method of measuring low temperature diffusivities in the Fe-Ni system with standard transmission electron microscope (STEM) based on diffusion couples study. They concluded that if the diffusion distances are less than the average grain size, the volume diffusion coefficients will not be influenced by grain boundary diffusion effects when the concentration profile is measured sufficiently far away from the grain boundaries. The reported diffusivity of Ni in their study is presented in Table 4.

Table 4: Low Temperature Diffusivity of Ni in the Fe-Ni system [44]

| Terminal Composition (wt%) | Temperature (°C) | Time (Days) | \tilde{D} of Ni (cm ² /s) |
|----------------------------|------------------|-------------|--|
| Fe10.4Ni-Fe15.5Ni | 800 | 3 | 3.60×10^{-15} |
| | 757 | 24 | 2.30×10^{-16} |

Dean *et al.* [45] reported an exhaustive study of determining interdiffusion coefficients in the Fe-Ni system between 925 °C and 600 °C in austenitic, γ by assembling diffusion couples. The values of diffusion coefficient, time, temperature, and terminal composition of the alloys investigated in the study are presented in Table 5.

Table 5: Diffusion Coefficient of Ni in the Fe-Ni Diffusion Couples [45]

| Terminal Composition (wt.%) | Temperature (°C) | Time (days) | \tilde{D} of Ni (cm ² /s) |
|-----------------------------|------------------|-------------|--|
| Fe5Ni-Fe10Ni | 910 | ~1 | 2.7×10^{-14} |
| Fe5Ni-Fe10Ni | 850 | 1.75 | 4.4×10^{-15} |
| Fe15Ni-Fe20Ni | 705 | 40 | 1.6×10^{-6} |
| Fe20Ni-Fe25Ni | 650 | 121 | 1.2×10^{-17} |
| Fe25Ni-Fe30Ni | 610 | 62 | 4.0×10^{-18} |

The values of pre-exponential constant, D_0 and Activation energy, Q for volume diffusion coefficient in binary Fe-Ni austenite reported in the study are presented below in Table 6.

Table 6: Values of D_0 and Q in Binary Fe-Ni Austenite [45]

| Temp. Range (°C) | Wt. % Ni | D_0 (cm ² /s) | Q (kJ/mol) |
|------------------|----------|----------------------------|-------------------|
| 1450 – 1050 | 4 | 0.44 ± 0.11 | 283.29 ± 3.13 |
| | 14 | 0.51 ± 0.12 | 281.58 ± 3.13 |
| 950 -750 | 25 | 0.33 | 251.04 |
| 1100 -950 | 10 | 2.85×10^3 | 350.21 |
| | 20 | 2.32×10^2 | 320.92 |
| 1426 - 705 | 10 | 0.2 | 264.43 |
| | 20 | 0.2 | 263.59 |

Ustad et al. [46] studied Fe-Ni, Fe-Co, and Ni-Co systems by making diffusion couples and investigated the temperature and concentration dependence of interdiffusion coefficients as well as the activation energies for a wide range of temperatures using electron probe microanalysis. The interdiffusion coefficient was observed to increase significantly with Ni concentration for all the temperatures above ~1000 °C. The interdiffusion coefficients in the Fe-Ni system determined in the study for a wide range of temperatures in the γ phase are presented below in Table 7.

Table 7: Concentration Dependence of Diffusion Coefficients of Ni in Fe-Ni system [46].

| System | Temperature Range (°C) | \bar{D} of Ni (10^{-11} cm ² /s) | | | | | | | | |
|--------|------------------------|--|------|------|------|------|------|------|------|------|
| | | at. % of Ni in Fe-Ni system | | | | | | | | |
| | | 10 | 20 | 30 | 40 | 50 | 60 | 70 | 80 | 90 |
| Fe-Ni | 705 | - | 0.27 | 0.25 | 0.26 | 0.26 | 0.27 | 0.30 | 0.33 | 0.33 |
| | 850 | 0.71 | 0.48 | 0.46 | 0.55 | 0.67 | 0.82 | 0.91 | 0.85 | 0.68 |
| | 1000 | 0.75 | 0.66 | 0.49 | 0.63 | 1.13 | 1.88 | 2.24 | 2.44 | 2.35 |
| | 1110 | 0.99 | 1.70 | 3.28 | 4.66 | 7.45 | 11.6 | 15.6 | 16.9 | 10.3 |
| | 1160 | 2.68 | 4.22 | 7.08 | 11.4 | 17.6 | 23.9 | 28.6 | 32.6 | 32.2 |
| | 1230 | 6.14 | 11.9 | 21.2 | 31.1 | 45.4 | 67 | 86.3 | 95.7 | 95.1 |
| | 1325 | 30 | 35 | 69.4 | 107 | 148 | 222 | 285 | 325 | 300 |
| | 1426 | 78.3 | 142 | 221 | 351 | 448 | 685 | 895 | 1032 | 960 |

Arifin *et al.* [47] investigated the diffusion of Ni at the liquid NiTi interface at temperatures of 2000, 2200, 2400, and 2600K for 1 ns using molecular dynamics (MD) simulations. MD simulations were performed using a large-scale atomic/molecular massively parallel simulator (LAMMPS) code. NVT Noose-Hover thermostat (a deterministic algorithm for constant temperature molecular dynamics solutions) was used to perform the simulations. The entire system consisted of 4000 atoms of each liquid Ni and liquid Ti and the liquid structures were produced by heating the Ni and Ti crystalline configuration at 2000 K (higher than the melting point of both Ni and Ti) for 100 ps. For the simulation a box in $35.2 \text{ \AA} \times 35.2 \text{ \AA} \times 185.2 \text{ \AA}$ dimensions was considered. To avoid diffusion along the crystal boundaries, periodic boundary conditions were set in all directions and the box was kept in vacuum. The diffusion coefficient was determined from the mean squared displacement (MSD) over the simulation time for the 200 atoms near the interface. The reported diffusion coefficient of Ni for 1 ns of MD simulation at 2000 K, 2200 K, 2400 K and 2600 K, were 7.44×10^{-5} cm²/s, 7.97×10^{-5} cm²/s, 1.02×10^{-4} cm²/s, and 1.05×10^{-4} cm²/s respectively. Activation energy was calculated using the Arrhenius equation and it was observed to 0.29 eV for Ni.

Yakubovich et al. [48] studied the diffusion process at the interface of pure Ni and Ti crystals and derived the diffusion coefficient of pure Ni in the temperature range of 500-700 K using classical molecular dynamics simulations. The simulation time was 3 ns and Langevin thermostat was used to achieve the temperature control. The systems consisted of 1301 Ni and 690 Ti atoms, and the interface geometry was optimized using periodic boundary conditions. The boundary atoms of the systems were frozen to avoid diffusion along the crystal boundaries. The diffusion coefficients of Ni at the Ni-Ti interface for 3 ns of MD simulation at 500 K, 600 K and 700 K were 2.53×10^{-8} cm²/s, 4.07×10^{-8} cm²/s and 2.00×10^{-7} cm²/s respectively. The diffusion coefficient has exponential dependence on the temperature and thus activation energy can be calculated using Arrhenius equation and the reported activation energy of Ni was 0.501 eV.

Atomic diffusion coefficients in liquid metals are difficult to measure experimentally which might be evaluated by quantum mechanics based theoretical modeling. One such approach was investigated by Walbrühl et al. [49] where they calculated the temperature dependent diffusion coefficients for Ni self-diffusion and seven binary Ni-X systems where (X = C, Co, N, Nb, Ta, Ti, W) using *ab initio* molecular dynamical simulations (AIMD). In liquid Ni-Co system at 1903 K, the reported diffusion coefficient of Ni and Co at Ni-10 at. % Co, Ni-50 at. % Co, and Ni- 90 at. % Co was 4.8×10^{-9} m²/s and 4.1×10^{-9} m²/s, 4.0×10^{-9} m²/s and 3.7×10^{-9} m²/s, and 2.9×10^{-9} m²/s and 4.8×10^{-9} m²/s, respectively.

Meyer et al. [50] reported an experimental technique to measure self-diffusion coefficients in liquid Ni via electromagnetic levitation with quasi-elastic neutron scattering. It was a container-less processing to avoid buoyancy driven convective fluid flow and chemical reaction of the liquid with container material. The experimental setup allowed them to measure the atomic self-motion in liquid Nickel within T_m (Ni = 1726K) \pm 200K. The reported self-diffusion coefficients of Ni

determined by quasi elastic neutron scattering is presented in Table 8. The Arrhenius fit of the self-diffusion coefficients data with respect to the inverse temperature resulted in an activation energy of 0.47 eV.

Table 8: Self-diffusion coefficients of Ni determined by quasi neutron elastic scattering [50].

| Temperature (K) | D (10^{-9} m ² /s) |
|-----------------|----------------------------------|
| 1514 \pm 5 | 2.09 \pm 0.08 |
| 1621 \pm 5 | 2.68 \pm 0.12 |
| 1750 \pm 5 | 3.47 \pm 0.06 |
| 1810 \pm 5 | 3.68 \pm 0.07 |
| 1870 \pm 5 | 4.05 \pm 0.20 |
| 1940 \pm 5 | 4.54 \pm 0.23 |

The experimental study of Ni-W system by Leonard et al. [51] yielded diffusion coefficient of W and Mo in liquid Ni in the temperature range 1755 - 2022 K and it was observed to be $2.4 \pm 0.7 \times 10^{-9}$ m²/s, and $1.6 \pm 0.7 \times 10^{-9}$ m²/s respectively. The liquid phase diffusion coefficients of W and Mo in liquid Ni were determined using a pulsed ion-beam melting technique and numerical simulation. A high intensity beam of nitrogen ions was focused on Ni substrate that was implanted with known concentration profile of W and Mo resulting in melting of the surface to a depth of 1 μ m.

Chathoth et al. [52] investigated self-diffusion of Ni in liquid Ni, Ni₈₀P₂₀, Pd₄₀Ni₄₀P₂₀, Pd₄₃Ni₁₀Cu₂₇P₂₀ via incoherent quasielastic neutron scattering. Mixing in general has a drastic effect on the liquidus temperature and the undercooling capabilities, however, no significant relationship between these properties and atomic diffusion in the liquid was observed. The underlying statement that diffusive motion is governed by packing fraction of the atoms, was observed to be true in these dense liquids as well. Self-diffusion coefficient of Ni in pure Ni at 1795 K was reported to be $3.8 \pm 0.06 \times 10^{-9}$ m²/s.

2.5 Purpose of this Doctoral Dissertation

This doctoral dissertation focuses on fabricating SS316L/IN718 bimetallic structures with emphasis on the compositional redistribution, phase transformation, and microstructural development that takes place after LPBF to provide a fundamental understanding of the fabrication process. Constituent intermixing after LPBF was quantitatively estimated using thermo-kinetic coefficients of mass transport. The intermixing observed and quantified in the SS316L/IN718 bimetallic structures represents the intermixing of constituent alloying elements in all LPBF processes. In addition, to understand the high temperature behavior, SS316L/IN718 bimetallic structures were annealed at 850 °C, 950 °C, and 1050 °C, for 120h, 48h, and 24h respectively, followed by water quenching. Furthermore, to better understand the intermixing of individual components (Ni and Fe) and to predict the varying (maximum) temperatures in LPBF of SS316L/IN718 bimetallic structures, SS316L vs IN718 diffusion couples were assembled by utilizing two extreme ends (i.e., SS316L and IN718 XY cross section) of SS316L/IN718 bimetallic structures. The SS316L vs IN718 diffusion couples were then annealed at 850 °C, 950 °C, and 1050 °C, for 120h, 48h, and 24h respectively, followed by water quenching. As an extension of this work, compositional redistribution, phase transformations and microstructural development, and nanohardness variations after LPBF of SS316L/IN625 bimetallic structure were also examined to provide a better understanding of the LPBF process via bimetallic fabrication.

CHAPTER 3: METHODOLOGY

3.1 LPBF of SS316L/IN718 Bimetallic Structure

Commercial SS316L and IN718 powders were acquired from SLM Solutions (SLM Solutions Group AG, Lübeck, Germany). The powder size distribution was examined using laser diffraction particle size analyzer (Beckman Coulter LSTM 13 320). The powder particle size for SS316L and IN718 was in the range of 19 - 46 μm and 18 - 49 μm , respectively. Chemical composition analysis of the powders was performed using x-ray energy-dispersive spectroscopy (XEDS) equipped on field emission scanning electron microscope FE-SEM (FE-SEM, Zeiss Ultra-55TM; Zeiss USA, White Plains, NY, USA), and compared with the nominal compositions from the OEM (SLM Solutions). They are both listed in Table 9, and Table 10, respectively. The secondary electron micrographs of the virgin SS316L and IN718 powders employed in the fabrication of SS316L/IN718 bimetallic structures are presented in Figure 1.

Table 9: Chemical Composition (wt. %) of SS316L powders determined by XEDS.

| | Fe | Cr | Ni | Mo | Mn | Si |
|------|---------------------|---------------------|---------------------|--------------------|--------------------|--------------------|
| OEM | Bal. | 16-18 | 10-14 | 2.0-3.0 | 2.0 | 1.0 |
| XEDS | 64.93 \pm 0.33 | 18.86 \pm 0.10 | 11.98 \pm 0.15 | 2.21 \pm 0.09 | 1.11 \pm 0.22 | 0.91 \pm 0.03 |

Table 10: Chemical Composition (wt. %) of IN718 powders determined by XEDS.

| | Fe | Cr | Ni | Nb | Mo | Co | Al | Mn | Ti | Si |
|------|--------------------|--------------------|--------------------|-------------------|-------------------|-------------------|------------------|-------------------|-------------------|-------------------|
| OEM | Bal. | 17-21 | 50-55 | 4.75- 5.50 | 2.8- 3.30 | 1.0 | 0.20- 0.80 | 0.35 | 0.65- 1.15 | 0.35 |
| XEDS | 18.9 \pm 0.59 | 20.4 \pm 0.18 | 51.3 \pm 0.59 | 4.6 \pm 0.59 | 2.5 \pm 0.21 | 0.1 \pm 0.17 | 1.0 \pm 0.2 | 0.1 \pm 0.09 | 1.0 \pm 0.16 | 0.2 \pm 0.09 |

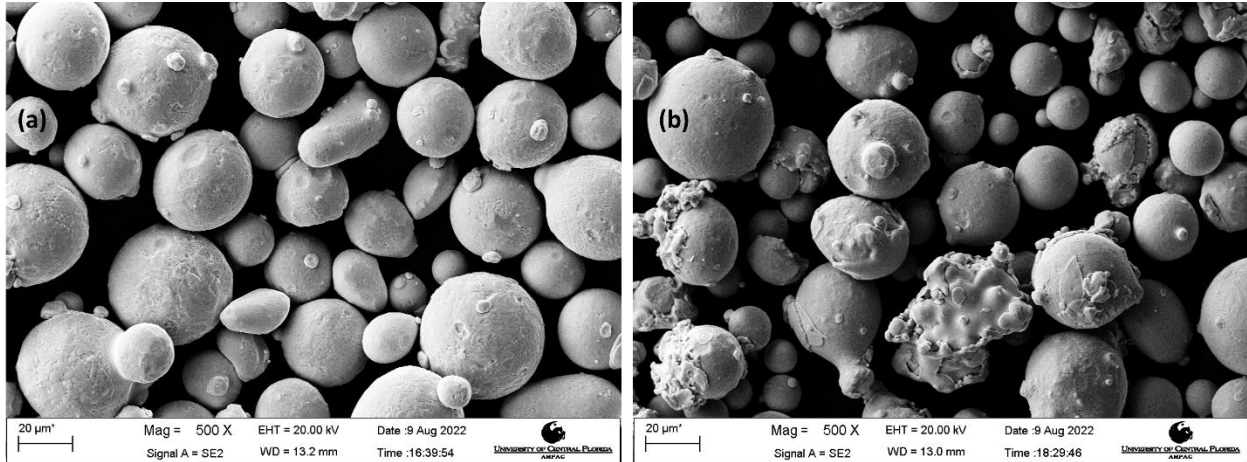


Figure 1: Secondary electron (SE) micrographs of virgin (a) SS316L and (b) IN718 powders

For LPBF of SS316L/IN718 bimetallic structures, an SLM 125^{HL} (SLM Solutions Group AG, Lubeck, Germany) was utilized. The SLM 125^{HL} is equipped with a continuous-wave (1070 nm wavelength) 400-W Ytterbium IPG fiber laser with a Gaussian spot size of $\sim 70 \mu\text{m}$ and a maximum build rate of $25 \text{ cm}^3/\text{h}$ [53]. Cylinders with a diameter of 10 mm, and height of 12 mm as presented in Figure 2, were manufactured using a laser power of 200 W, laser scan speed of 800 mm/s, hatch spacing of 0.12 mm, slice thickness of 0.03 mm, layer rotation of 45° and stripe pattern of 10 mm width. Scanning strategies such as bordering or contouring were not employed. The cylinders were built onto SS316L build plate for minimum thermal mismatch and good thermal conduction. The build plate was preheated to 100°C . The build was performed in an inert Ar atmosphere (ultra-high purity Ar) with an O_2 content lower than 0.10 %. The SS316L/IN718 bimetallic structures were fabricated based on the following steps [54]: (1) design the CAD file of the bimetallic structures, (2) employ the optimized processing parameters and transfer the *.stl* file to the LPBF machine, (3) fill the reservoir with virgin SS316L powders, (4) start the build using standard operating procedures, (5) layer by layer building of SS316L cylinders on SS316L build plate for 200 layers, until the desired height of 6 mm is reached, (6) pause the process, (7) remove

SS316L powders from powder feed reservoir and downpipe loader, (8) re-filling the reservoir with virgin IN718 powders, and (8) resume the process to complete the build.

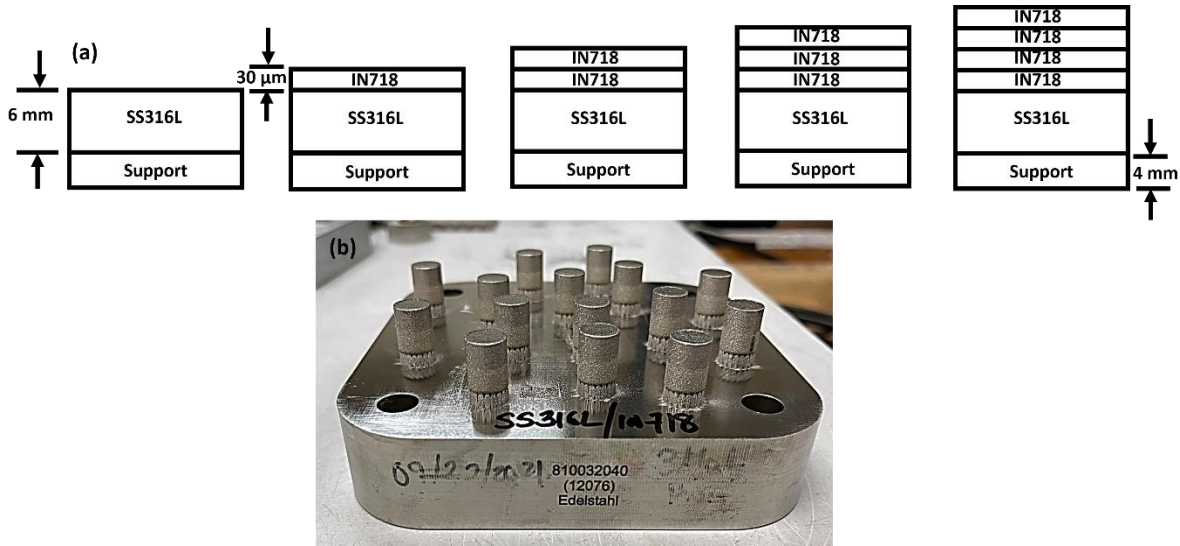


Figure 2: (a) A schematic of the layer-by-layer fashion of fabrication of bimetallic structures via LPBF. A slice thickness of $30\ \mu\text{m}$ was used to build both SS316 and IN718 to 6 mm in height; (b) Fabricated SS316L/IN718 bimetallic structures. The diameter and height of the cylinders were 10 mm and 12 mm, respectively.

3.2 SS316L vs IN718 Diffusion Couples from SS316L/IN718 Bimetallic Structure

For SS316L vs IN718 diffusion couples assembly, two ends of the SS316L/IN718 bimetallic structure were sectioned into discs approximately 2.5 mm in thickness and 10 mm in diameter using a low-speed diamond saw and metallographically polished down to $1\ \mu\text{m}$ surface finish. The polished surfaces were placed in contact with each other and were held together by two clamping disks with rods made of Invar steel [55–60]. The couples were then placed in quartz capsules, sealed on one end, evacuated to 1×10^{-6} torr, and flushed with ultrahigh-purity Argon. The evacuation and hydrogen flush were repeated several times, and the capsule was finally filled

with ultrahigh-purity Argon. The final Argon pressure in the capsule was controlled so that the pressure inside the capsule was approximately 1 atm at the annealing temperatures. The capsule was then sealed and placed at the center of a Lindberg /Blue (Asheville, NC) three zone tube furnace. The furnace ends were fully insulated to minimize temperature gradients. Three diffusion couples were prepared and were annealed at 850 °C isothermally for 120h, 950 °C for 48h and 1050 °C for 24h, respectively. These diffusion couples were quenched in water by breaking the quartz capsules to preserve the high temperature microstructure. The samples were then mounted in epoxy, cross sectioned and metallographically polished down to 1 μm surface finish for characterization.

3.3 Heat Treatment of SS316L/IN718 Bimetallic Structure

For the heat treatment purpose, two ends of the SS316L/IN718 bimetallic structure were sectioned and the interface cross section was utilized. The SS316L/IN718 interface cross sections were then placed in quartz capsules, sealed on one end, evacuated to 1×10^{-6} torr, and flushed with ultrahigh-purity Argon. The evacuation and hydrogen flush were repeated several times, and the capsule was finally filled with ultrahigh-purity Argon. The final Argon pressure in the capsule was controlled so that the pressure inside the capsule was approximately 1 atm at the annealing temperatures. The capsule was then sealed and placed at the center of a Lindberg /Blue (Asheville, NC) three zone tube furnace. To test and understand the high temperature behavior of SS316L/IN718 bimetallic structures, the specimens were annealed at 850 °C, 950 °C, 1050 °C for 120 h, 48 h and 24 h respectively. After annealing, all the specimens were water quenched to preserve the high temperature microstructure followed by sectioning for further characterization.

3.4 LPBF of SS316L/IN625 Bimetallic Structure

Commercial SS316L and IN625 powders were acquired from SLM Solutions (SLM Solutions Group AG, Lübeck, Germany). The powder size distribution was examined using laser diffraction particle size analyzer (Beckman Coulter LSTM 13 320). The powder particle size for SS316L and IN625 was in the range of 19 - 46 μm and 21 - 46 μm , respectively. The secondary electron micrographs of the powders employed in the fabrication of SS316L/IN625 bimetallic structures are presented in Figure 3.

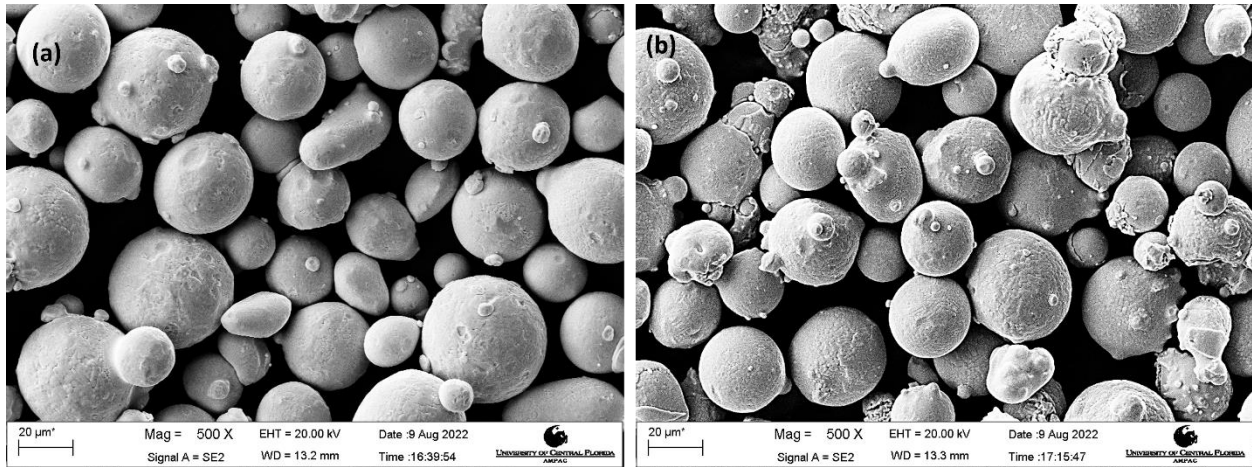


Figure 3: Secondary electron micrographs of virgin (a) SS316L and (b) IN625 powders.

For LPBF of SS316L/IN625 bimetallic structures, an SLM 125^{HL} (SLM Solutions Group AG, Lübeck, Germany) was utilized. The SLM 125^{HL} is equipped with a continuous-wave (1070 nm wavelength) 400-W Ytterbium IPG fiber laser with a Gaussian spot size of $\sim 70 \mu\text{m}$ and a maximum build rate of 25 cm^3/h . Cylinders with a diameter of 10 mm and height of 12 mm as presented in Figure 4 were manufactured using a laser power of 200 W, laser scan speed of 800 mm/s, hatch spacing of 0.12 mm and slice thickness of 0.03 mm, layer rotation of 45° and stripe pattern of 10 mm width. Scanning strategies such as bordering or contouring were not employed.

The cylinders were built onto SS316L build plate for minimum thermal mismatch and good thermal conduction. The build plate was preheated to 100 °C. The build was performed in an inert Ar atmosphere (ultra-high purity Ar) with an O₂ content lower than 0.10 %. The SS316L/IN625 bimetallic structures were fabricated based on the following steps: (1) design the CAD file of the bimetallic structures, (2) employ the optimized processing parameters and transfer the *.stl* file to the LPBF machine, (3) fill the reservoir with virgin SS316L powders, (4) start the build using standard operating procedures, (5) layer by layer building of SS316L cylinders on SS316L build plate for 200 layers, until the desired height of 6 mm is reached, (6) pause the process, (7) remove SS316L powders from powder feed reservoir and downpipe loader, (8) re-filling the reservoir with virgin IN625 powders, and (8) resume the process to complete the build.



Figure 4: Fabricated SS316L/IN625 bimetallic structures. The diameter and height of the cylinders were 10 mm and 12 mm, respectively.

3.5 Phase Constituents and Microstructure Analysis

After the print, the samples were cross sectioned using a low-speed diamond saw. Each sample sectioned was mounted in epoxy and prepared using standard metallographic techniques. All samples were given a final polishing using 1 μm diamond paste and colloidal silica (0.05 μm) polishing suspension. Once the final polishing was completed, bimetallic interface cross section was examined using the Nikon Metaphot optical microscope to investigate the crack/pores near or at the interface. The SS316L/IN718 and SS316L/IN625 interface cross section was then etched with mixed acids, which consists of HCl, acetic acid and HNO_3 with the volume ratio of 3:2:1.

FE-SEM equipped with XEDS was used to examine the surface morphology, cross-sectional phase constituents and microstructure of the interface cross section. Both the secondary electrons (SE) and backscattered electron (BSE) imaging modes were utilized. A minimum of three concentration profiles, across the interface of the bimetallic structures and diffusion couples were obtained by point-to-point acquisition to study the intermixing profile and diffusion profile of the alloying constituents. XEDS data were converted to the concentration of various constituent elements in atom percent via standardless analysis.

X-ray diffraction (XRD) was carried out for phase identification and preferred crystallographic orientation analysis using a PANalytical Empyrean™ diffractometer with Cu target $\text{K}\alpha$ radiation operating at 45 kV and 40 mA. A step size of 0.03° and a counting duration of 90 seconds were employed for a good resolution and statistical significance.

3.6 Mechanical Properties via Nanohardness Test

Metallographically polished samples down to 1 μm surface were subjected to hardness measurements. Quasi-static nanoindentation was performed with a Berkovich tip using a Hysitron™ TI Premier nanoindenter on the specimens. Nanoindentation was carried out at 5000

μN peak load with 10 s of loading time, 3 s of holding at the peak load, and 10 s of unloading. Hardness (H) and Reduced Modulus (E_r) were determined by analyzing the unloading part of the load-displacement curve using Oliver and Pharr's method [35, 36]. Young's modulus (E) was estimated from the reduced modulus (E_r) using [35].

$$\frac{1}{E_r} = \frac{1-\nu^2}{E} + \frac{1-\nu_i^2}{E_i} \quad (2)$$

where, E_r is the reduced modulus of the specimen, E_i is Young's modulus of the diamond indenter tip (1140 GPa), ν is the Poisson's ratio of the specimen and ν_i is the Poisson's ratio of the diamond indenter tip (0.07). 200-250 linear indents with a spacing of 20 μm were performed to determine the mechanical properties of the bimetallic interfaces via nanoindentation.

CHAPTER 4: RESULTS AND DISCUSSIONS

4.1 LPBF of SS316L/IN718 Bimetallic Structure

4.1.1 Phase Constituents and Microstructure:

XRD patterns from the section normal to the build direction, XY (i.e., from SS316L and IN718) are presented in Figure 5. The main peaks observed from both the cross sections corresponded to the austenitic γ (fcc) matrix as indexed in Figure 5. All the peaks were indexed by comparing with the powder diffraction files in PANalytical HighScore software. As the bimetallic interface region was observed to be less than 1 mm, the XRD pattern from this region did not yield any significant difference. However, the lattice parameter determined through expanded Rietveld refinement for SS316L, SS316L/IN718 interface region, and IN718 cross sections were observed to be 3.6075 Å, 3.6162 Å and 3.6100 Å, respectively. According to JCPDS-ICDD® data files, the lattice parameter of FCC AISI 316L austenitic stainless steel is 3.60 Å [61]. Woo et al. [62] reported a single FCC structure with lattice parameters (a_o) of AM SS316L to be 3.596 Å via *In situ* neutron diffraction study. Mahadevan et al. [63] reported the lattice parameter of austenitic matrix in IN718 to be 3.62 Å,

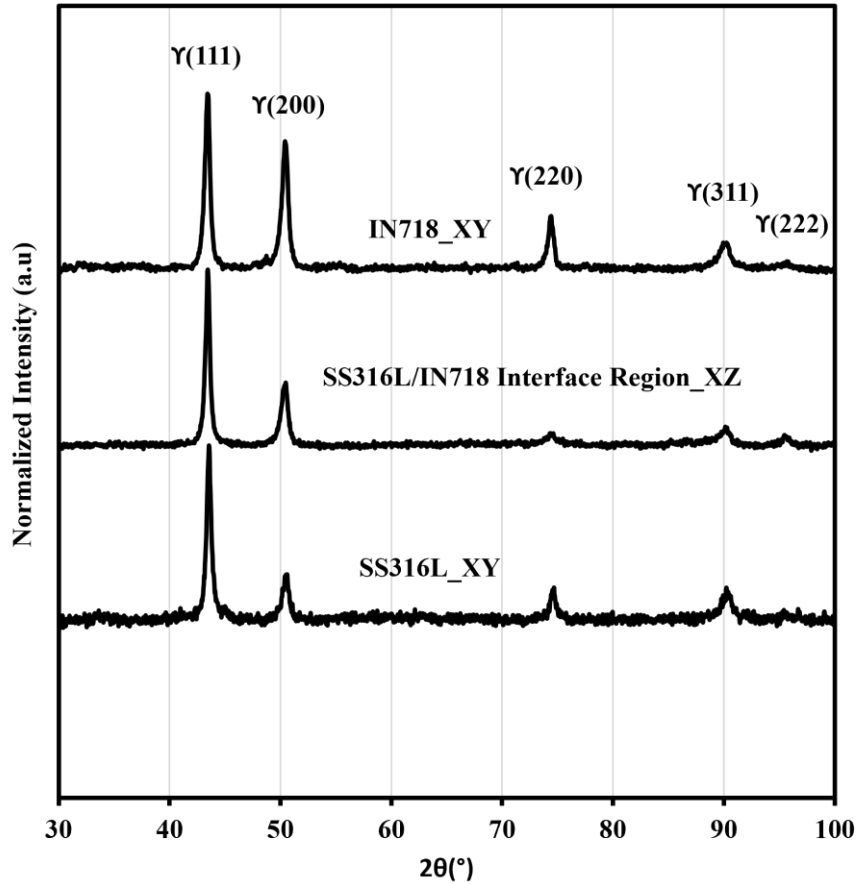


Figure 5: X-ray diffraction patterns of SS316L_XY, IN718_XY, and SS316L/IN718 interface region_XZ cross sections collected from fabricated SS316L/IN718 bimetallic structure.

No cracks were observed at the interface cross section of SS316L/IN718 bimetallic structures and only a few pores were noticeable as shown by the unetched optical micrograph in Figure 6(a). Negligible porosity observed at the interface region indicates sound metallurgical bonding between the two alloys, and demonstrates that the bimetallic structures manufactured by LPBF technique are nearly fully dense.

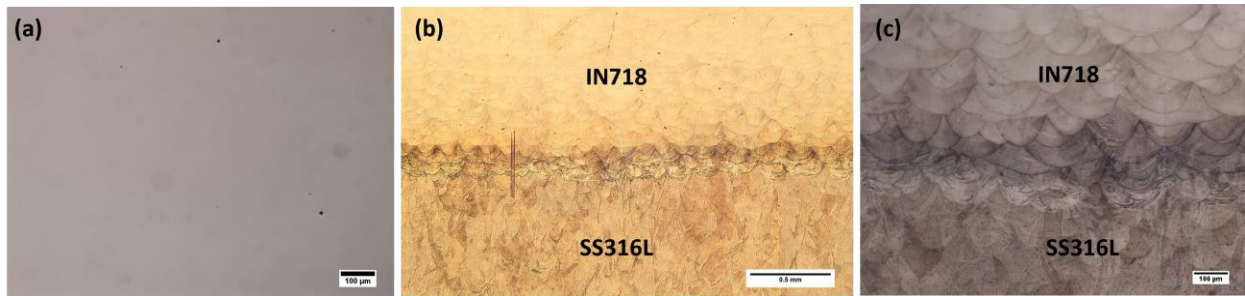


Figure 6: Optical Micrographs of SS316L/IN718 interface cross section: (a) unetched, (b) low magnification etched and (c) high magnification etched.

The low and high magnification etched, cross-sectional optical micrographs at the interface region are presented in Figure 6(b) and Figure 6(c), respectively. The interface region consisted of well-developed semicircular overlapped SS316L and IN718 melt pools, and the interface width measured using ImageJ was observed to be approximately 200 μm .

Scanning electron micrographs at high and low magnification in Figure 7 show the representative details of the microstructure and phase constituents at or near the SS316L/IN718 bimetallic interface. IN718 has a higher average atomic number making it appear brighter than SS316L as presented in Figure 7(a). The microstructure near the interface region of the SS316L/IN718 bimetallic structure consisted of typical cellular/columnar structure as presented in Figure 7(b). Also, the interdendritic region appeared with continuous white contrast compared to the dark contrast of the dendritic core, typically due to the segregation of heavier elements. Figure 7(c) revealed the presence of nanoscale Laves phase (indicated by arrows) and carbides (indicated by circles) near the interface of the SS316L/IN718 bimetallic structure, consistent with those reported by Mohd Yusuf et al. [64]. Typically, LPBF of as-fabricated IN718 alloy consists of fine cellular or columnar dendritic microstructure resulting from the rapid cooling rate. In general, Nb, Mo and Ti segregate along the cellular boundary and interdendritic region resulting in the formation of nanoscale Laves and carbides. Precipitates of Υ' or Υ'' were not observed in the as-

fabricated IN718 alloy. The formation of the Laves phase occurs through the eutectic reaction $L \rightarrow \gamma + \text{Laves}$ and is typically enriched with Nb [65,66]

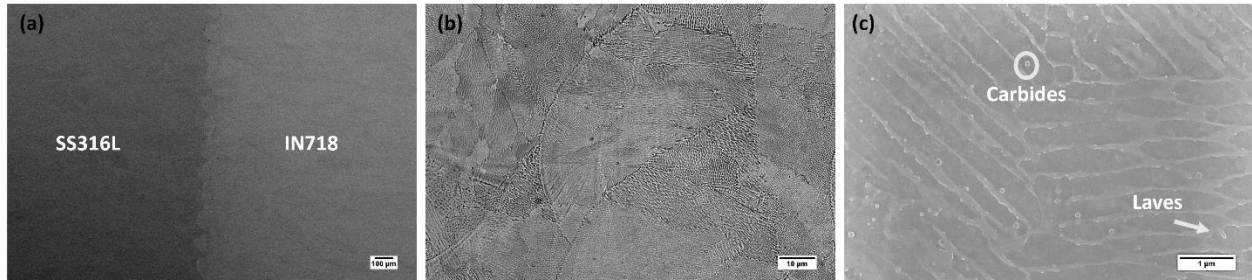


Figure 7: Electron micrographs of SS316L/IN718 bimetallic interface cross section: (a) low magnification BSE micrographs revealing the entire cross section, (b) backscattered electron micrographs revealing the cellular/columnar microstructure of the interface, (c) high magnification micrographs revealing the cellular/columnar microstructure along with the carbides and laves phases.

4.1.2 Constituent Intermixing and Nanohardness

Figure 8 (a) shows the cross-sectional concentration profiles of Fe, Ni and Cr across the SS316L/IN718 bimetallic interface, indicating significant intermixing of Ni and Fe. No significant change in Cr concentration was observed because Cr concentration is similar for SS316L and IN718 alloys. Variation in laser power or scan speed can play a significant role in intermixing at the interface region. For example, varying the laser power from 1.2 kW to 2 kW while keeping the other laser processing parameters constant, widening of the compositional gradient up to 3.5 mm was observed when IN625 was deposited upon SS316L fabricated on mild steel substrate via DED [41].

In binary diffusion, typically, the chemical composition varies in the interdiffusion zone. Therefore, diffusing species continuously experience different chemical surroundings, and

because the intermixing rate will depend on concentration, it too will vary throughout the intermixing zone. For such systems, Boltzmann [67] and Matano derived an integro-differential equation to calculate the interdiffusion at any given composition and is given by [68]

$$\tilde{D} = \frac{\frac{1}{2t} \int_{C_i^{\pm\infty}}^{C^0} (x-x_0) dC}{\frac{\partial C}{\partial x}} \quad (3)$$

where $C^{+\infty}$ and $C^{-\infty}$ refer to the composition at terminal ends of the diffusion couple, x_0 is the position of the Matano plane, and C^0 is the composition at the Matano plane.

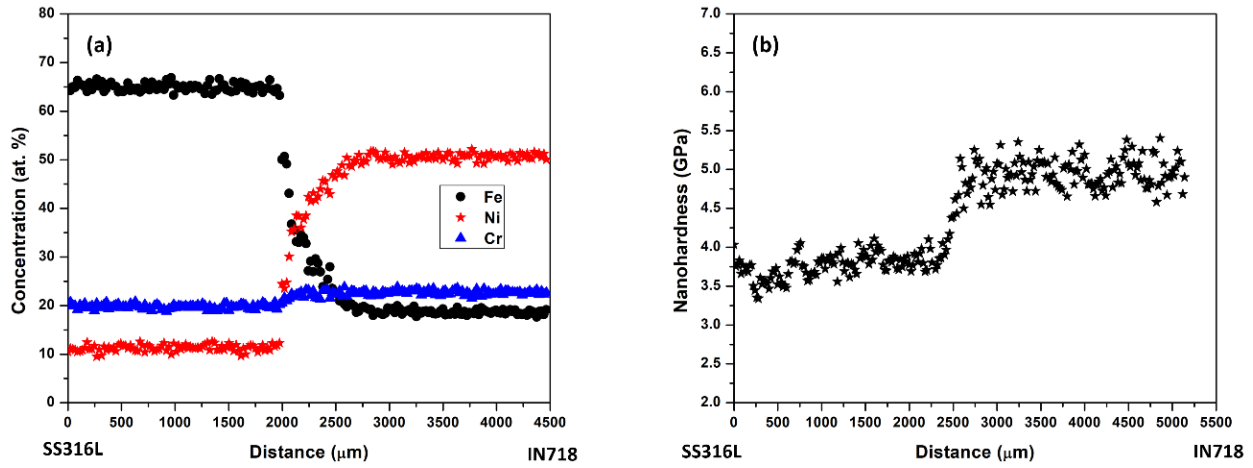


Figure 8: Concentration profiles of Fe, Ni and Cr, and (b) Nanohardness profile in the vicinity of SS316L/IN718 bimetallic interface.

The Matano plane denotes the location of mass balance such that:

$$\int_{C^{+\infty}}^{C^0} x dC + \int_{C^0}^{C^{-\infty}} x dC = 0 \quad (4)$$

The intermixing fluxes of individual components, including the influence of convection may be determined directly from their concentration profiles without the need of the thermo-kinetic intermixing coefficients by [55]:

$$\tilde{J}_i = \frac{1}{2t} \int_{C_i^{\pm\infty}}^{C_i(x)} (x - x_0) dC_i \quad (i = 1, 2, 3 \dots n) \quad (5)$$

where t is the time. In LPBF process, the laser, due to its small beam diameter (50-600 μm) interacts with a small region (0.002 mm^2 – 0.28 mm^2) of the powder bed resulting in very high-power density ($>10^4 \text{ W/mm}^2$) [69]. Such high-power density yields an extremely high heating rate followed by rapid cooling (10^4 K/s – 10^7 K/s). The predicted time temperature relationship in a single laser study reported by Pantawane et al. [69] indicated varying cooling behavior within a temperature range of 3315 K - 578 K in a time frame of 1 ms. Their result provides insight into the fact that the potential intermixing time for specimens produced by LPBF could be in the 1 ms range.

To estimate the intermixing time for specimens produced by LPBF we used the concept of laser residence. In LPBF, the laser residence time is the time of interaction of laser beam at a particular location during scanning and is given by $t_r = d/v$ where d is the beam diameter and v is the scan speed of the laser. For the SS316L/IN718 bimetallic structures fabricated by SLM 125^{HL} PBF unit, beam diameter (spot size) was 70 μm (approximately) and employed scan speed was 800 mm/s which yields a laser residence time of 875 μs for a layer thickness of 70 μm [21] (average melt pool depth was observed to be approximately 70 μm with a laser power of 200W and 800 mm/s). The estimated residence time is very close to 1 ms, the same as that reported by Pantawane et al. [69]. Significant intermixing of Fe and Ni was observed within 800 μm (intermixing zone) based on the concentration profiles presented in Figure 8(a). So, the intermixing region basically went through a heat treatment (i.e., annealing) for a period of $\frac{800 \mu\text{m}}{70 \mu\text{m}} \times 875 \mu\text{s} \sim 10 \text{ ms}$.

As the intermixing coefficient typically varies over the composition range, Dayananda [70] proposed an average effective interdiffusion coefficient which provides a single nominal thermo-kinetic coefficient for the compositional spectrum and allows for comparison with other constant

coefficients. Integrating the intermixing flux (\tilde{J}_i) over an interval from x_1 to x_2 , and dividing by the change in composition over the interval, yields the average effective interdiffusion coefficient, as:

$$\widetilde{D^{eff}} = \frac{\int_{x_1}^{x_2} \tilde{J} dx}{c_{x_2} - c_{x_1}} \quad (6)$$

This average effective interdiffusion was used to calculate the intermixing coefficient of Ni and Fe in SS316L/IN718 bimetallic structures. Intermixing of primary solvents, Ni and Fe was observed for a diffusion zone of 800 μm approximately (Figure 8a), and the intermixing coefficient of Ni and Fe was estimated to be $6.5 \times 10^{-5} \text{ m}^2/\text{s}$ and $6.0 \times 10^{-5} \text{ m}^2/\text{s}$, respectively, based on the time of 10 ms. However, Figure 9 presents the intermixing coefficient of Ni and Fe as a function of time. In addition, the measured diffusivity of Ni in different solid-state Fe-Ni diffusion couples are presented and compared in Table 11 with the intermixing coefficient of Ni in SS316L/IN718 bimetallic structure fabricated by LPBF.

The mechanical properties of the SS316L/IN718 bimetallic structure derived from instrumented nanoindentation are presented in Figure 8(b). In general, IN718 has higher hardness than SS316L while interface region was observed to have hardness in between the IN718 and SS316L structure. Typically, the nanohardness of additively manufactured SS316L ranges from $3.4 \pm 0.69 \text{ GPa}$ to $3.7 \pm 0.64 \text{ GPa}$ [71]. Zhou et al. [3] reported the nanohardness of as-built IN718 fabricated by LPBF to be $4.9 \pm 0.13 \text{ GPa}$. Ghanavati et al. [30] reported a tensile strength of 581.72 MPa and ductility of 33.5 % for SS316L/IN718 bimetallic structure fabricated by LPBF.

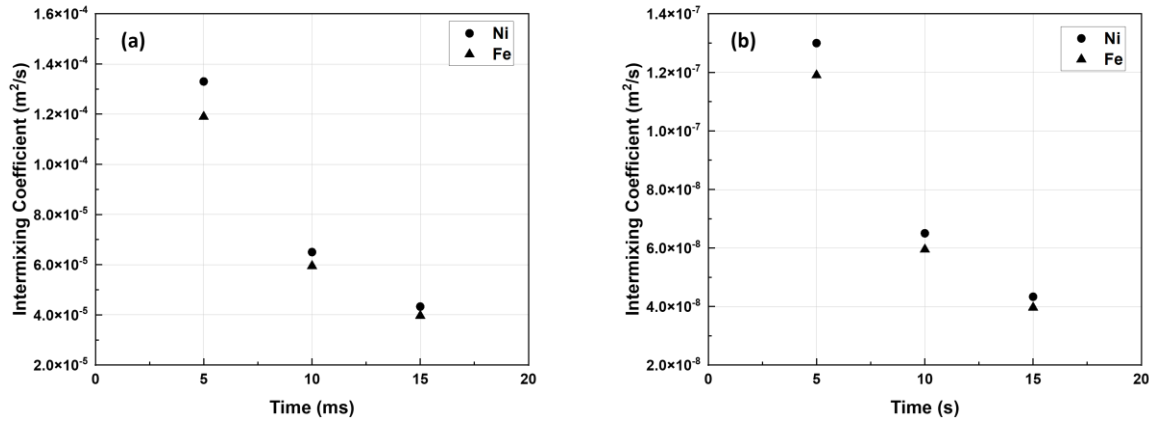


Figure 9: Intermixing coefficient of Ni and Fe as a function of time in SS316L/IN718 bimetallic structures: (a) Time in ms, (b) Time in s

Table 11: Diffusion coefficient of Ni in Fe-Ni diffusion couples and intermixing coefficient estimated in SS316L/IN718 bimetallic structure produced by LPBF.

| Fabrication Technique | Terminal Composition (wt.%) | Temperature (°C) | Time (days) | \tilde{D} of Ni (m ² /s) | Ref. |
|-----------------------|-----------------------------|------------------|-------------|---------------------------------------|------------|
| Diffusion Couple | Fe5Ni-Fe10Ni | 910 | ~1 | 2.7×10^{-18} | [45] |
| | Fe5Ni-Fe10Ni | 850 | 1.75 | 4.4×10^{-19} | [45] |
| | Fe10Ni-Fe15Ni | 802 | 3 | 3.6×10^{-19} | [44] |
| | Fe10Ni-Fe15Ni | 757 | 24 | 2.3×10^{-20} | [44] |
| | Fe15Ni-Fe20Ni | 705 | 40 | 1.6×10^{-20} | [45] |
| | Fe20Ni-Fe25Ni | 650 | 121 | 1.2×10^{-21} | [45] |
| | Fe25Ni-Fe30Ni | 610 | 62 | 4.0×10^{-22} | [45] |
| LPBF | SS316L/IN718 Bimetallic | Varying | 10 ms | 6.5×10^{-5} | This study |

4.2 Heat Treatment of SS316L/IN718 Bimetallic Structures Fabricated by LPBF

To understand the high temperature behavior, SS316L/IN718 bimetallic structures were annealed at 850 °C, 950 °C, and 1050 °C, for 120h, 48h, and 24h respectively, followed by water quenching. Figure 10 presents the concentration profile of Fe, Ni and Cr in the vicinity of SS316L/IN718 bimetallic interface before and after annealing.

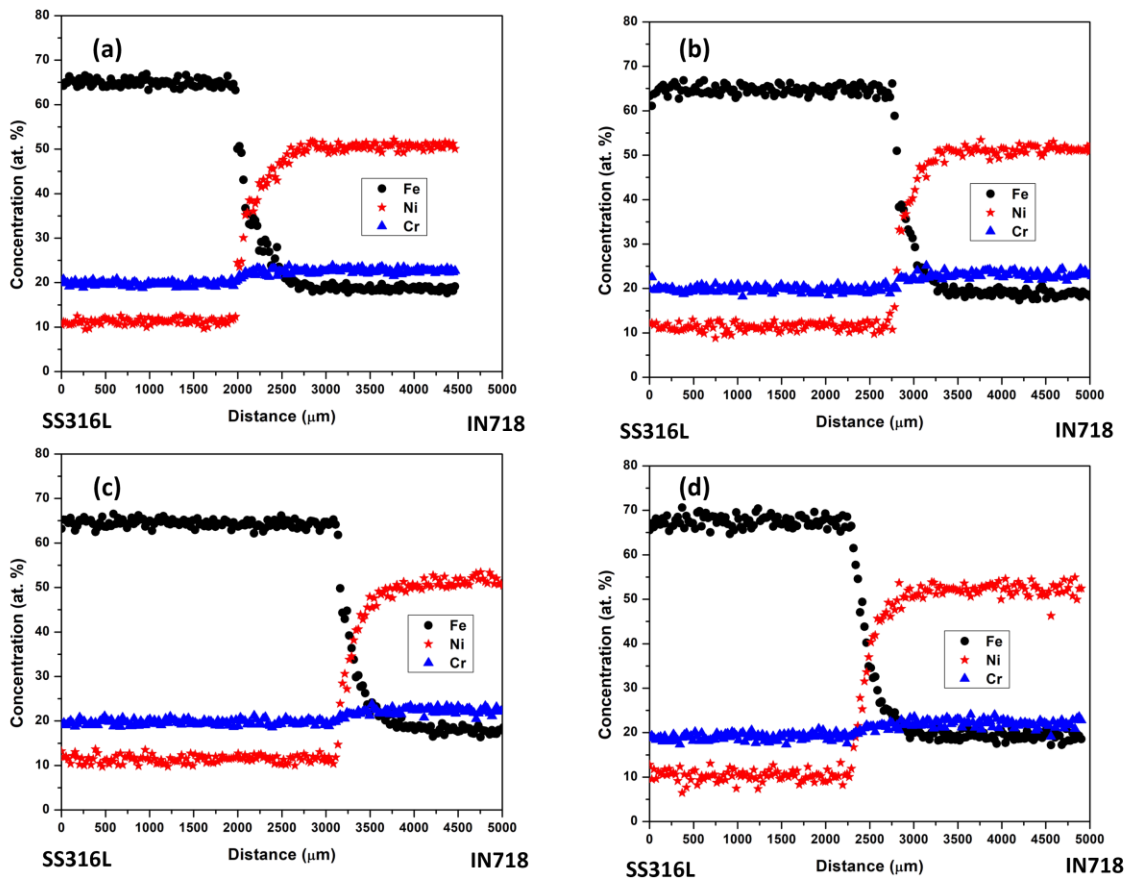


Figure 10: Concentration profiles of Fe, Ni, and Cr in the vicinity of SS316L/IN718 bimetallic interface before and after annealing: (a) As fabricated, (b) 850 °C for 120h, (c) 950 °C for 48h, and (d) 1050 °C for 24h followed by WQ.

Dayananda [72] reported that the concentration profiles of the individual components for a single-phase multicomponent diffusion couple with n components may be analyzed in terms of the relative concentration variable Y_i which is defined as:

$$Y_i = \frac{c_i - c_i^+}{c_i^- - c_i^+} \dots\dots\dots ()$$

where C_i is the concentration in g moles/cc of the component i at any section of the diffusion zone.

The relative concentration of the constituent elements (Ni and Fe) has been utilized to determine

the diffusion zone of the as fabricated and annealed SS316L/IN718 bimetallic structures from the relative concentration profile as presented in Figure 11.

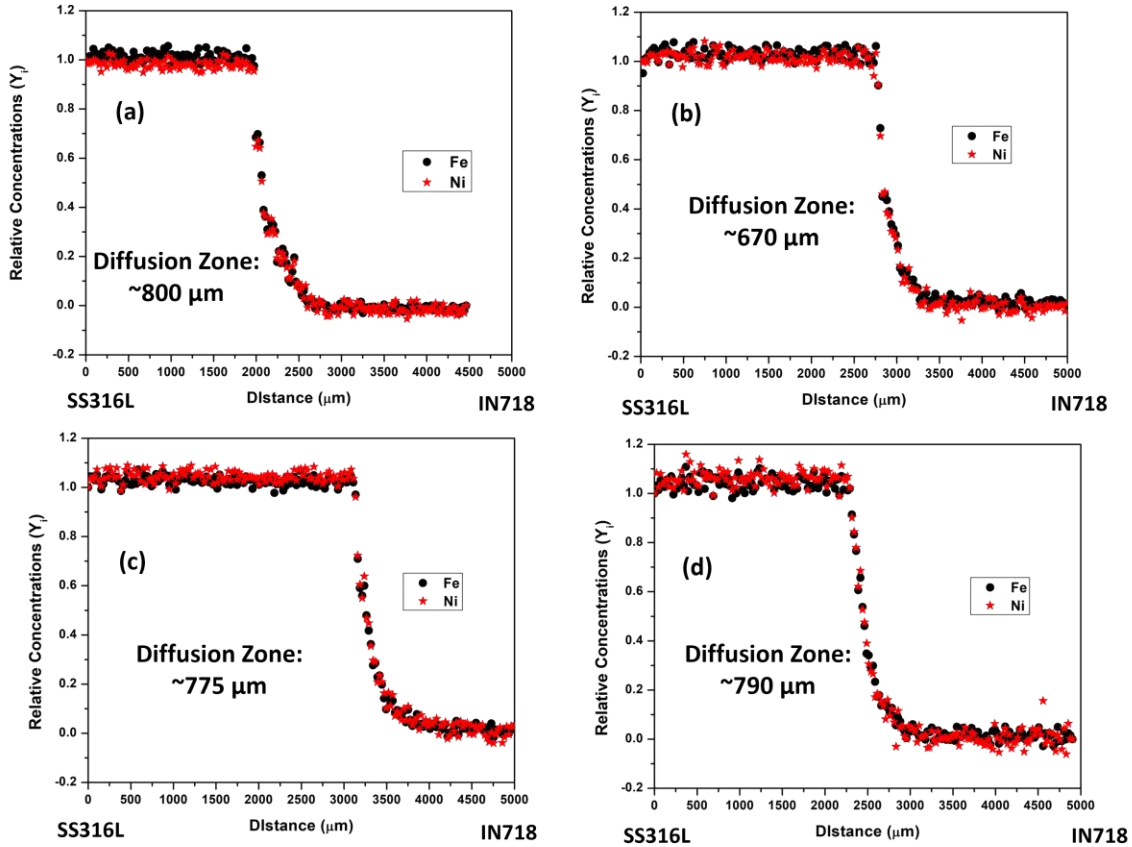


Figure 11: Concentration profiles of Fe and Ni expressed in terms of relative concentration in the vicinity of annealed SS316L/IN718 bimetallic interface: (a) As-fabricated, (b) 850 °C for 120h, (c) 950 °C for 48h, and (d) 1050 °C for 24h followed by WQ.

Elsaß et al. [73] reported a detailed investigation of the temperature influence on the development of interdiffusion phenomena in MCrAlY-coated nickel-based superalloys. They annealed NiCoCrAlYSi bond coated (BC1) Renè 80 and CM 247 at 950 °C, 980 °C, 1050 °C for up to 10,000 hours. Their study revealed that after identical annealing times, at higher temperature more nickel has diffused out of the substrate (i.e., Renè 80 and CM 247) than at lower temperature (i.e., at identical annealing time, the diffusion width of nickel was significantly higher at higher

temperature when compared to lower temperature). The diffusion zone of the annealed SS316L/IN718 bimetallic structures in our study was observed to increase with the increase in temperatures. However, the as-fabricated SS316L/IN718 bimetallic structure showed the maximum diffusion zone of approximately 800 μm . This warrants further investigation to understand the variation in diffusion zone between the as-fabricated and annealed bimetallic structures. Figure 12 presents the etched optical micrographs of the SS316L/IN718 bimetallic interface cross section before and after annealing.

The electron micrographs of the SS316L and IN718 ends from the SS316L/IN718 bimetallic structures revealed the change in microstructure due to annealing and are presented in Figure 13. As presented in Figure 13(a, b), both the SS316L and IN718 ends produced cellular or columnar structure before annealing and is consistent with the literature [16,21]. Plate like precipitates (identified as δ) within the grains and along the grain boundaries and precipitates of γ'' (needle shaped morphology) were potentially observed after annealing at 850 $^{\circ}\text{C}$ for 120 h at the IN718 end as presented in Figure 13(c) [3,65,66,74].

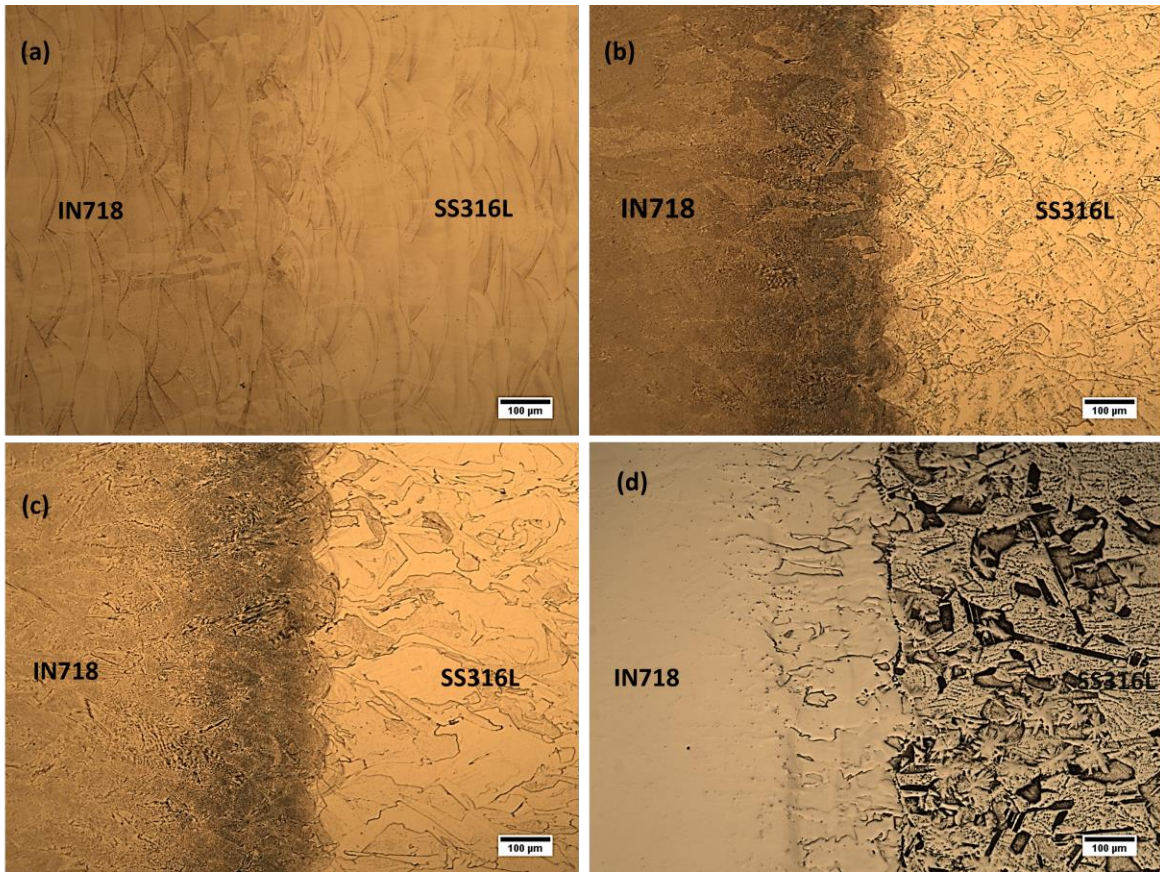


Figure 12: Etched optical micrographs of SS316L/IN718 bimetallic interface cross section before and after annealing: (a) As-fabricated, (b) 850 °C for 120h, (c) 950 °C for 48h, and (d) 1050 °C for 24h followed by WQ.

Figure 13(d) indicated the presence of potential δ (plate like precipitates) and γ'' (needle shaped) at the SS316L end after annealing at 850 °C for 120h. After annealing at 950 °C for 48h, at the IN718 end, the cellular structure appeared to grow larger, however, many δ precipitates with a plate morphology developed near the cellular or grain boundary region. The temperature was not high enough to completely dissolve the laves phase and few needles shaped precipitates identified as γ'' were observed [3].

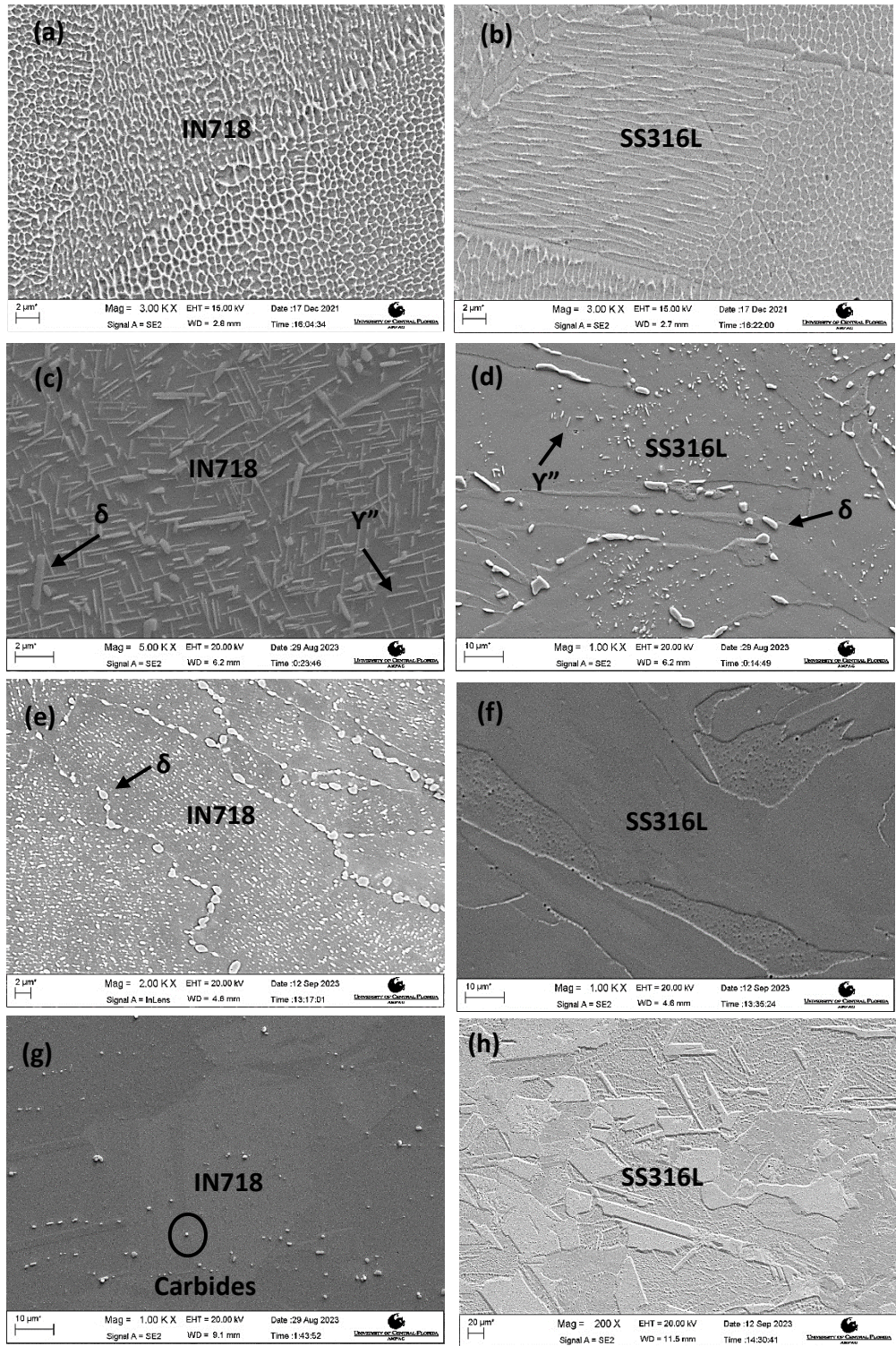


Figure 13: Electron micrographs demonstrating the change in microstructure before and after annealing of SS316L/IN718 bimetallic structure: (a, b) As-fabricated, (c, d) 850 °C for 120h, (e, f) 950 °C for 48h, and (g, h) 1050 °C for 24h followed by WQ.

The cellular structure of the as-fabricated SS316L produced before annealing were no longer observed and the melt pool boundaries dissolved after annealing at 950 °C for 48h [75,76]. Figure 13(g) indicates recrystallization, dissolution of laves phases, potential grain growth and precipitation along grain boundaries potentially carbides after annealing at 1050 °C for 24h [3,65,66] for IN718 end. The SS316L end exhibited potential grain growth indicating potential recrystallization [75].

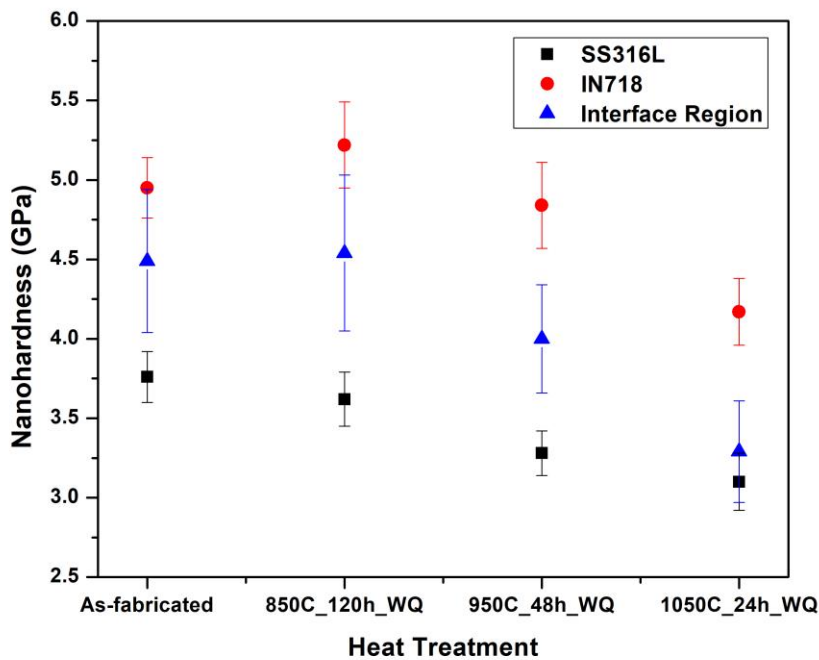


Figure 14: Nanoindentation Hardness of SS316L, SS316L/IN718 bimetallic interface region, and IN718 before and after annealing.

Figure 14 presents the nanoindentation hardness of the SS316L/IN718 bimetallic structure before and after annealing. IN718 end of the bimetallic structure showed the maximum hardness after annealing at 850 °C for 120 h potentially due to formation of γ'' precipitates as presented in Figure 14 and indicated in Figure 13(c). The IN718 end of the bimetallic structure showed slightly lower

hardness after annealing at 950 °C for 48h compared to as the as-fabricated one potentially due to reduction of dislocation density owing to removal of residual stress [77]. Due to complete dissolution of fine cellular structure and recrystallization at 1050 °C, IN718 end showed the lowest nanohardness consistent with the findings as indicated in Figure 13(g). The interface region of the SS316L/IN718 bimetallic structure exhibited a similar trend like IN718 end.

4.3 SS316L vs IN718 Diffusion Couples from SS316L/IN718 Bimetallic Structures

SS316L vs IN718 diffusion couples were assembled by utilizing two extreme ends (i.e., SS316L and IN718 cross section) of SS316L/IN718 bimetallic structures. To better understand the high temperature behavior of SS316L/IN718 bimetallic structure and intermixing of individual components (Ni and Fe), SS316L vs IN718 diffusion couples were annealed at 850 °C, 950 °C, and 1050 °C, for 120h, 48h, and 24h respectively, followed by water quenching. It is worth mentioning that the annealing temperature, time, and quenching media were kept same for the heat treatment of SS316L/IN718 bimetallic structures and diffusion couple assembly. Diffusion couple technique has been chosen for the validation purpose as it is a powerful and viable technique in establishing phase relationships and the efficiency of this method in general is very high [78]. Excellent diffusion bonding was achieved for the SS316L vs IN718 diffusion couples annealed at 850 °C for 120h, 950 °C for 48h, and 1050 °C for 24h, respectively as shown in Figure 15. The concentration profile and corresponding interdiffusion fluxes of Ni and Fe collected from SS316L vs IN718 diffusion couples are presented in Figure 16.

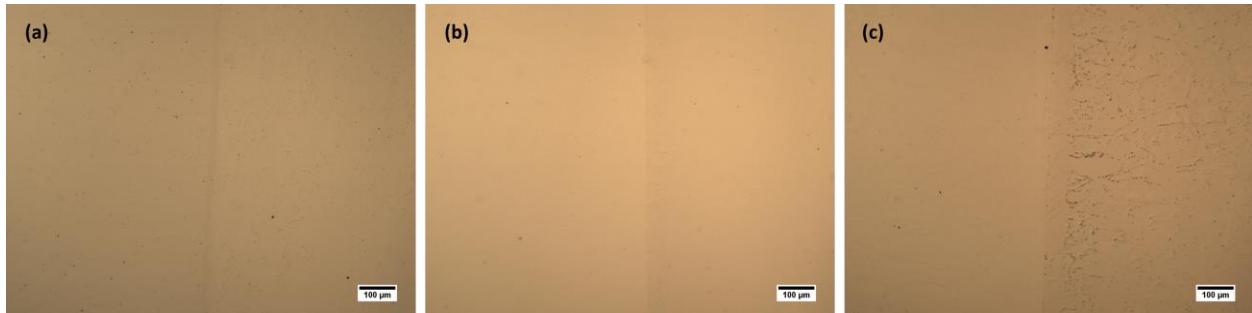


Figure 15: Unetched optical micrographs of the interface microstructure of SS316L vs IN718 diffusion couples annealed at (a) 850 °C for 120h, (b) 950 °C for 48h, and (c) 1050 °C for 24h followed by WQ.

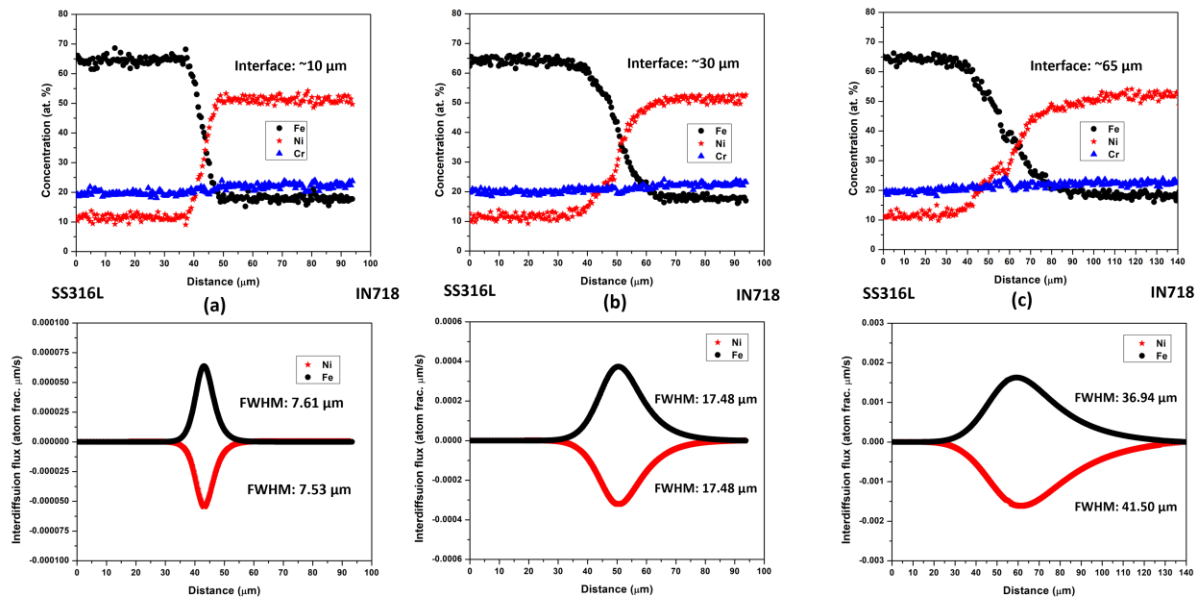


Figure 16: Concentration profile and corresponding interdiffusion fluxes of Ni and Fe from SS316L vs IN718 diffusion couples annealed at (a) (a) 850 °C for 120h, (b) 950 °C for 48h, and (c) 1050 °C for 24h followed by WQ.

The etched microstructure of SS316L vs IN718 diffusion couples annealed at 850, 950, and 1050 °C, for 120, 48, and 24 h respectively, followed by WQ are presented in Figure 17. These microstructures are very similar to the annealed SS316L/IN718 bimetallic microstructures as

presented in Figure 12 except that the diffusion zone observed in the SS316L vs IN718 diffusion couples are shorter compared to the annealed SS316L/IN718 bimetallic structures.



Figure 17: Etched optical micrographs of the interface microstructure of SS316L vs IN718 diffusion couples annealed at (a) 850 °C for 120h, (b) 950 °C for 48h, and (c) 1050 °C for 24h followed by WQ.

The average effective interdiffusion coefficients of Ni and Fe in SS316L vs IN718 diffusion couple in the temperature range from 850 to 1050 °C was determined using the same approach as discussed in section 4.1.2

Figure 18 presents the corresponding Arrhenius plot for the temperature dependence of average effective interdiffusion coefficients within the temperature range of 850 to 1050 °C for SS316 vs IN718 diffusion couples. The average effective interdiffusion coefficients, activation energies, and pre-exponential factor of Ni and Fe determined from the SS316L vs IN718 diffusion couples annealed at 850, 950, and 1050 °C are presented in Table 12 respectively.

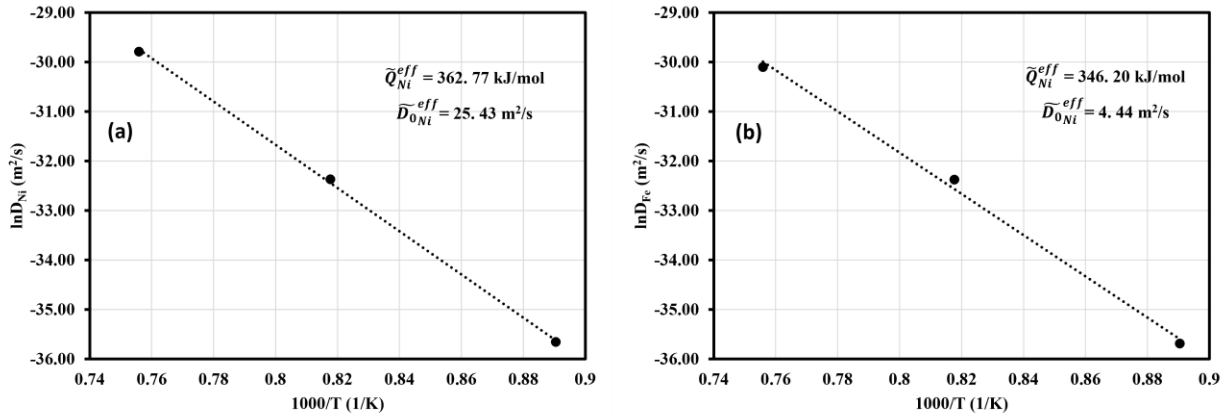


Figure 18: Temperature dependence of average effective interdiffusion coefficients for (a) Ni, and (b) Fe determined from SS316L vs IN718 diffusion couples in the temperature range from 850 to 1050 °C.

Table 12: Average effective interdiffusion coefficients and the corresponding Activation Energy and Pre-exponential factor of Ni and Fe determined from SS316L vs IN718 diffusion couple.

| Diffusion Couple | Temperature (°C) | \tilde{D}_{Ni}^{eff} (m ² /s) | \tilde{D}_{Fe}^{eff} (m ² /s) | \tilde{Q}_{Ni}^{eff} (kJ/mol) | \tilde{D}_{0Ni}^{eff} (m ² /s) | \tilde{Q}_{Fe}^{eff} (kJ/mol) | \tilde{D}_{0Fe}^{eff} (m ² /s) |
|------------------|------------------|--|--|---------------------------------|---|---------------------------------|---|
| SS316L vs IN718 | 850 | 3.28×10^{-16} | 3.17×10^{-16} | 362.77 | 25.43 | 346.29 | 4.44 |
| | 950 | 8.78×10^{-15} | 8.73×10^{-15} | | | | |
| | 1050 | 1.16×10^{-13} | 8.49×10^{-14} | | | | |

To compare and evaluate the activation energy of average effective interdiffusion coefficients of Ni determined from SS316L vs IN718 diffusion couple, existing literatures were investigated, and the results are presented in Table 13.

Table 13: Activation energy (Q) and Pre-exponential constant (D_0) extracted from relevant literatures and this study.

| Temp. Range (°C) | Diffusion Couple | Wt. % Ni | D_0 (cm ² /s) | Q (kJ/mol) | Ref. | |
|------------------|------------------|----------|----------------------------|-------------------|-------------------|------|
| 1450 – 1050 | Fe-Ni | 4 | 0.44 ± 0.11 | 283.29 ± 3.13 | [45] | |
| | | 14 | 0.51 ± 0.12 | 281.58 ± 3.13 | | |
| 950 -750 | | 25 | 0.33 | 251.04 | | |
| 1100 -950 | | 10 | 2.85×10^3 | 350.21 | | |
| | | 20 | 2.32×10^2 | 320.92 | | |
| 1426 - 705 | | 10 | 0.2 | 264.43 | | |
| | | 20 | | 263.59 | | |
| 1000 -1300 | | 50 | | 0.38 ± 0.25 | 317.45 ± 0.01 | [46] |
| 1150 - 1300 | | | | | 246.06 | |
| 1000 - 1426 | | | | | 256.67 ± 0.02 | |
| 850 - 1050 | SS316L vs IN718 | 12-51 | 25.43×10^4 | 362.77 | This study | |

Ustad et al [46] reported that the activation energies for the temperature range 1000 to 1426 °C were in good agreement with the published data for volume diffusion in the Fe-Ni system and no grain boundary diffusion was observed at that temperature range. However, for temperatures below 1000 °C, the diffusion coefficients showed less dependence on concentration and temperature resulting in smaller activation energy and grain boundary diffusion was observed to be the dominant diffusion mechanism.

In addition, the measured diffusivity of Ni in different solid-state Fe-Ni diffusion couples, the diffusion coefficient of Ni determined from SS316L vs IN718 diffusion couple study is presented and compared in Table 14 with the intermixing coefficient of Ni in the SS316L/IN718 bimetallic structure fabricated via LPBF.

Table 14: Diffusion coefficient of Ni in Fe-Ni and SS316L vs IN718 diffusion couples and intermixing coefficient estimated in SS316L/IN718 bimetallic structures produced via LPBF.

| Fabrication Technique | Terminal Composition (wt.%) | Temperature (°C) | Time (days) | \tilde{D} of Ni (m ² /s) | Ref. |
|-----------------------|-----------------------------|------------------|------------------------|---------------------------------------|------------|
| Diffusion Couple | Fe5Ni-Fe10Ni | 910 | ~1 | 2.70×10^{-18} | [45] |
| | Fe5Ni-Fe10Ni | 850 | 1.75 | 4.40×10^{-19} | [45] |
| | Fe10Ni-Fe15Ni | 802 | 3 | 3.60×10^{-19} | [44] |
| | Fe10Ni-Fe15Ni | 757 | 24 | 2.30×10^{-20} | [44] |
| | Fe15Ni-Fe20Ni | 705 | 40 | 1.60×10^{-20} | [45] |
| | Fe20Ni-Fe25Ni | 650 | 121 | 1.20×10^{-21} | [45] |
| | Fe25Ni-Fe30Ni | 610 | 62 | 4.00×10^{-22} | [45] |
| | SS316L vs IN718 | 850 | 5 | 3.28×10^{-16} | This study |
| | SS316L vs IN718 | 950 | 2 | 8.78×10^{-15} | This study |
| SS316L vs IN718 | 1050 | 1 | 1.16×10^{-13} | This study | |
| LPBF | SS316L/IN718 Bimetallic | Varying | 10 ms | 6.50×10^{-5} | This study |

The temperature dependence of diffusion coefficients can be described by Arrhenius relationship and was utilized to predict the varying (maximum) temperature in LPBF process:

$$D = D_0 \exp\left(\frac{-Q}{RT}\right) \quad (7)$$

Substituting the intermixing coefficient of Ni estimated in SS316L/IN718 bimetallic structures, $D_{Ni} = 6.50 \times 10^{-5}$ m²/s when $t = 10$ ms, activation energy, $\tilde{Q}_{Ni}^{eff} = 362.77$ kJ/mol and preexponential factor, 25.43 m²/s of Ni determined from SS316L vs IN718 diffusion couple, T was estimated to be ~ 3388 K. Temperatures up to or beyond 3000 °C were reported by Zhirnov et al. [79] in typical LPBF process.

Therefore, a temperature of ~ 3400 K observed in LPBF of SS316L/IN718 bimetallic structure calculated based on the diffusivity data from SS316L vs IN718 diffusion couple yields few concerns: (1) The temperature observed is significantly higher than melting point of both Ni (1726 K) [51] and Fe. (2) Potential liquid state diffusion to occur first followed by solid-state

diffusion in LPBF of SS316L/IN718 bimetallic structure or some other mechanism might be involved in the LPBF process.

Meyer et al. [50] reported an experimental technique to measure the self-diffusion coefficients of liquid metals in a wide temperature range that was not influenced by convection. They had reported self-diffusion coefficients of Ni determined by quasi elastic neutron scattering without the influence of convection within a temperature range of 1520 to 1945 K. Heterogenous nucleation at crucible walls were avoided because of which the melts can be undercooled below the equilibrium melting temperature such that diffusion data were also available in the metastable regime of an undercooled liquid. Figure 19 presents the self-diffusion coefficients of Ni as a function of inverse temperature from 1520 to 1945 K. Meyer's self-diffusion coefficients of Ni data has been extrapolated to 3400 K and is presented in Table 15. The self-diffusion coefficient of Ni at 3400 K was determined by extrapolating Meyer's self-diffusion coefficients of Ni data within 1520 to 1945 K temperature range and it was observed to be approximately 1.45×10^{-8} m²/s. The intermixing coefficient of Ni estimated in SS316L/IN718 bimetallic structure was observed to be 6.5×10^{-5} m²/s based on time of 10 ms. There is a difference of 3 orders of magnitude in the Ni self-diffusion coefficients at 3400 K when measured without the influence of convection. Thus, in addition to diffusion, convection might be involved in the LPBF process.

Based on the extrapolated self-diffusion coefficient of Ni (1.45×10^{-8} m²/s) at 3400 K, the period (time) during which the intermixing zone in SS316L/IN718 bimetallic structure fabricated via LPBF basically went through a heat treatment (i.e., annealing) was estimated, and it was observed to be approximately 6.51 s.

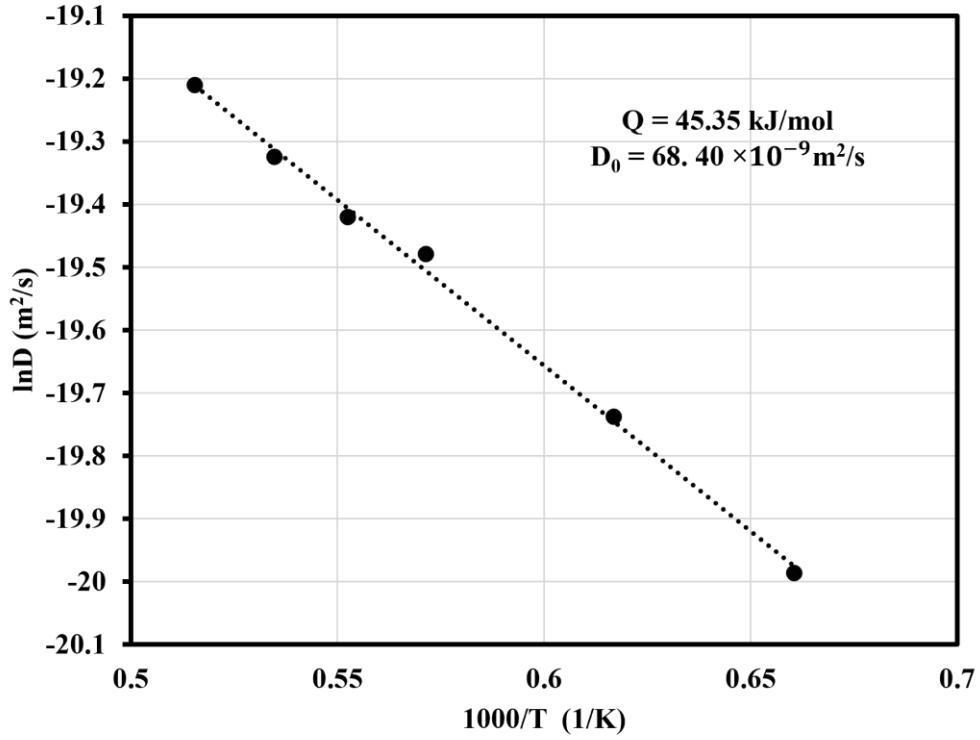


Figure 19: Temperature dependence of Ni self-diffusion coefficients in the temperature range of 1520 to 1945 K. This plot was done using Meyer’s Ni self-diffusion coefficients data.

Table 15: Extrapolation of Meyer et al. [50] self-diffusion coefficients of Ni to 3400 K.

| Temperature (K) | D (10^{-9} m ² /s) |
|-----------------|----------------------------------|
| 1514 ± 5 | 2.09 ± 0.08 |
| 1621 ± 5 | 2.68 ± 0.12 |
| 1750 ± 5 | 3.47 ± 0.06 |
| 1810 ± 5 | 3.68 ± 0.07 |
| 1870 ± 5 | 4.05 ± 0.20 |
| 1940 ± 5 | 4.54 ± 0.23 |
| ... | ... |
| ... | ... |
| 3000 | 1.17×10^{-8} |
| 3400 | 1.45×10^{-8} |

4.4 LPBF of SS316L/IN625 Bimetallic Structure

4.4.1 Phase Constituents and Microstructure:

XRD patterns from the section normal to the build direction, XY (i.e., from SS316L and IN625) are presented in Figure 20. The main peaks observed from both the cross sections corresponded to the austenitic γ (fcc) matrix as indexed in Figure 20. All the peaks were indexed by comparing with the powder diffraction files in PANalytical HighScore software. As the bimetallic interface region was observed to be less than 1 mm, the XRD pattern from this region did not yield any significant difference. However, the lattice parameter determined through expanded Rietveld refinement for SS316L, SS316L/IN625 interface region, and IN625 cross sections were observed to be 3.6075 Å, 3.6209 Å and 3.6098 Å, respectively. According to JCPDS-ICDD® data files, the lattice parameter of FCC AISI 316L austenitic stainless steel is 3.60 Å [61]. Woo et al. [62] reported a single FCC structure with lattice parameters (a_o) of AM SS316L to be 3.596 Å via *In situ* neutron diffraction study. Zhang et al. [80] reported the lattice parameter of matrix phase (i.e., FCC γ) in as-built AM IN625 to be 3.6033 ± 0.0768 Å using high resolution synchrotron XRD measurements.

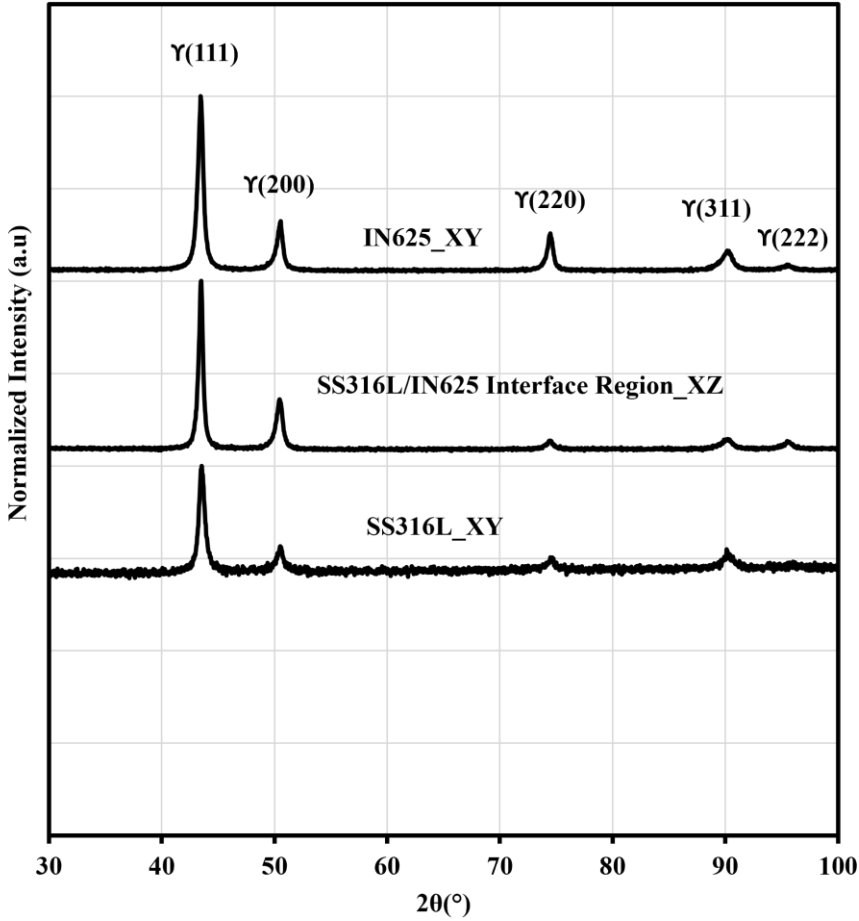


Figure 20: X-ray diffraction patterns of SS316L_XY, IN625_XY, and SS316L/IN625 interface cross sections collected from fabricated SS316L/IN625 bimetallic structure.

No cracks were observed at the interface cross section of SS316L/IN625 bimetallic structures and only a few pores were noticeable as shown by the unetched optical micrograph in Figure 21(a). Negligible porosity observed at the interface region indicates sound metallurgical bonding between the two alloys and demonstrates that the bimetallic structures manufactured by LPBF technique are nearly fully dense. The interface region consisted of well-developed semicircular overlapped SS316L and IN625 melt pools, and the interface width was observed to be approximately 100 μm as presented in Figure 21(b).

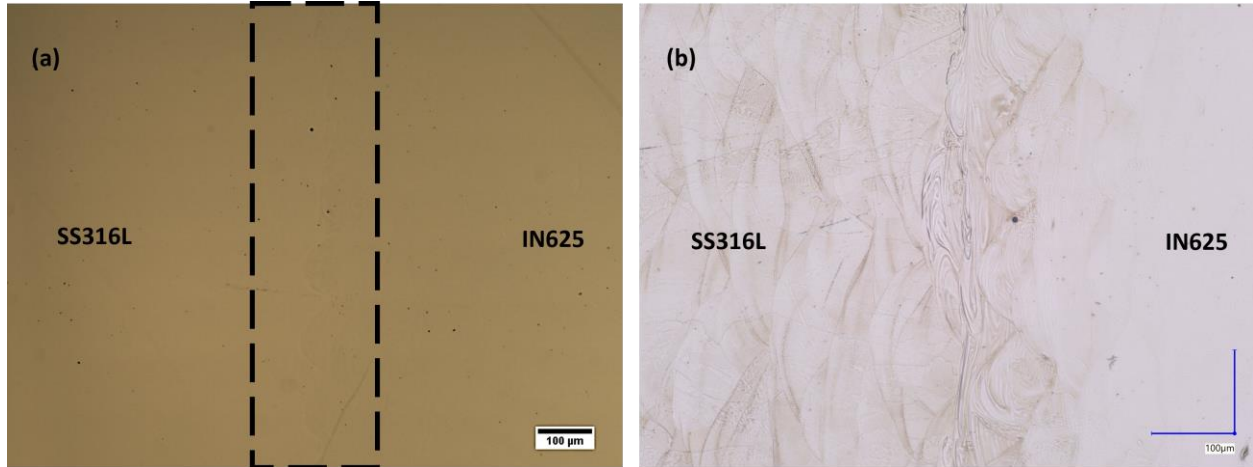


Figure 21: Optical Micrographs of SS316L/IN625 interface cross section: (a) unetched, (b) etched.

Scanning electron micrographs at high and low magnification in Figure 22 shows the representative details of the microstructure and phase constituents at or near the SS316L/IN625 bimetallic interface. IN625 has a higher average atomic number making it appear brighter than SS316L as presented in Figure 22(a). Figure 22(b) presents the overlapping of the melt pools at or near the interface region. The microstructure near the interface region of the SS316L/IN625 bimetallic structure consisted of typical cellular/columnar structure as presented in Figure 22(c). Figure 22(d) revealed the presence of potential nanoscale Laves phase (indicated by arrows) near the interface of the SS316L/IN625 bimetallic structure. Typically, LPBF of as-fabricated IN625 alloy consists of sub-grain cellular solidification structure with Nb and Mo segregation along the intercellular boundaries. In addition, A_2B Laves phase was identified to decorate the intercellular boundaries [81].

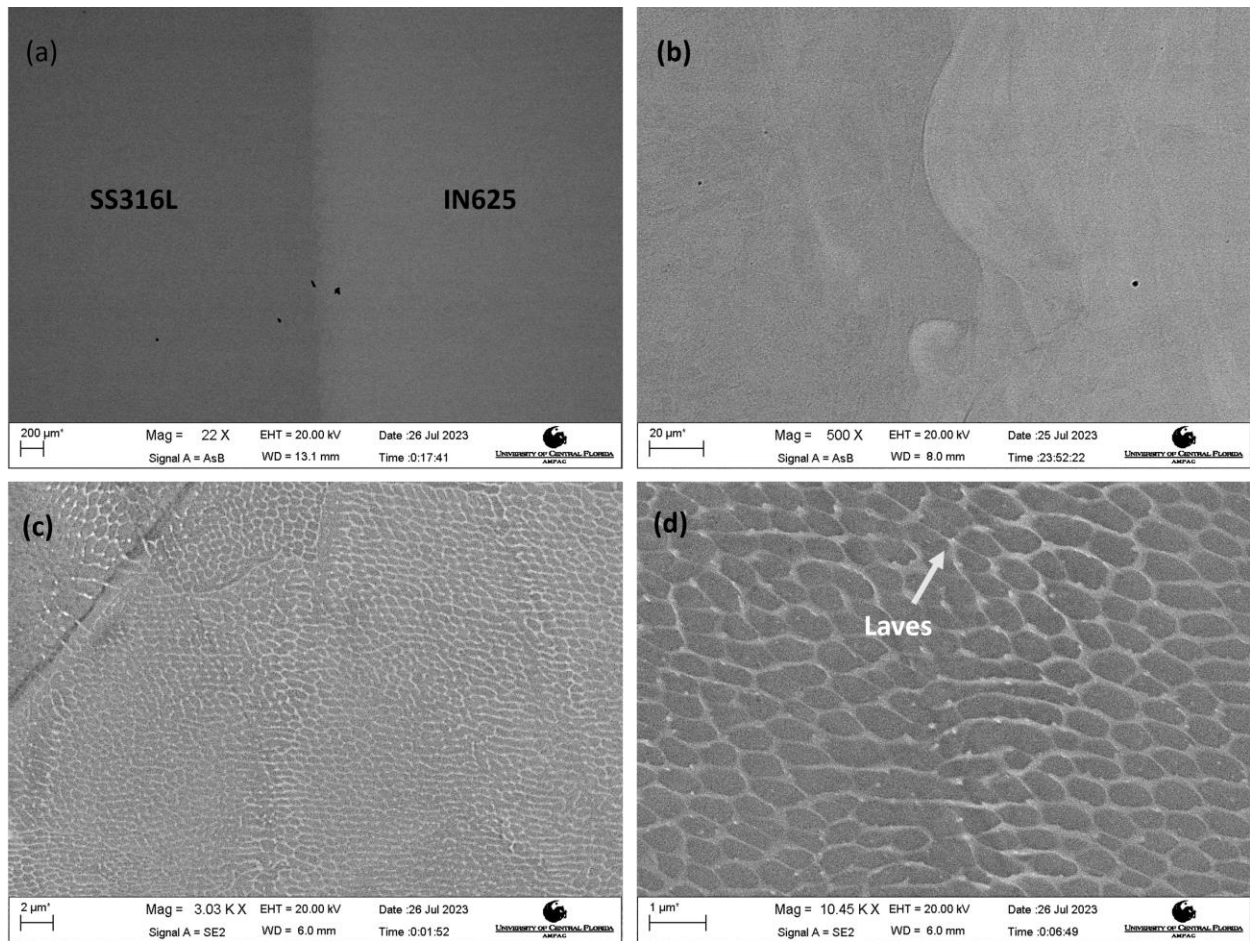


Figure 22: Electron micrographs of SS316L/IN625 bimetallic interface cross section: (a) low magnification BSE micrographs revealing the entire cross section, (b) BSE micrographs revealing the overlapping of the melt pools (c) high magnification SE micrographs revealing the cellular/columnar microstructure, and (d) high magnification SE micrographs revealing potential laves phases.

4.4.2 Constituents Intermixing and Nanohardness:

Figure 23(a) shows the cross-sectional concentration profiles of Fe, Ni, and Cr across the SS316L/IN625 bimetallic interface, indicating the significant intermixing of Ni and Fe. Little change in Cr concentration was observed because Cr concentration is almost similar for SS316L and IN625 alloys.

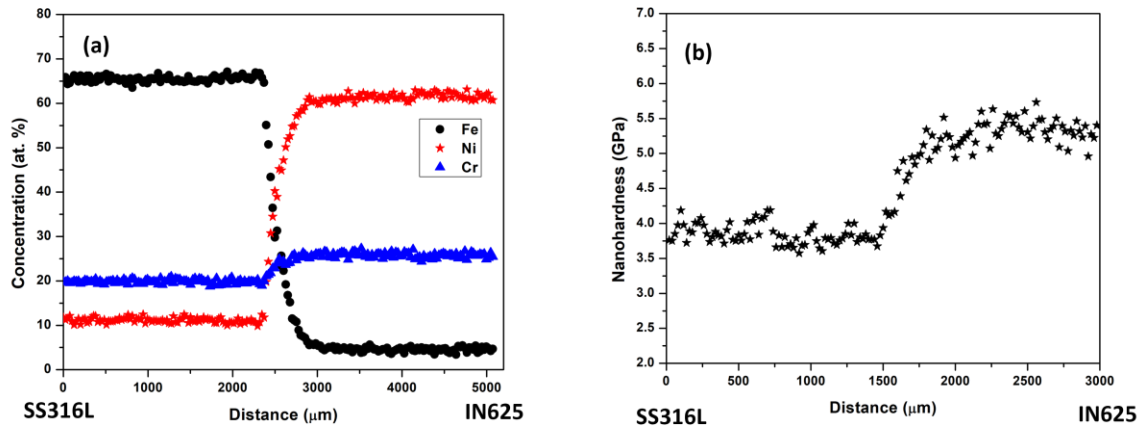


Figure 23: (a) Concentration profiles of Fe, Ni and Cr; (b) nanohardness profile in the vicinity of SS316L/IN625 bimetallic interface.

For the SS316L/IN625 bimetallic structures fabricated via the SLM 125^{HL} PBF unit, the beam diameter (spot size) was 70 μm (approximately), and the scan speed employed was 800 mm/s, which yielded a laser residence time of 875 μs for a layer thickness of 80 μm (average melt pool depth was observed to be approximately 80 μm, with a laser power of 200 W and 800 mm/s) [82]. The intermixing zone was observed to be approximately 600 μm based on the concentration profile in Figure 23(a). So, the intermixing region basically went through a heat treatment (i.e., annealing) for a period of $\frac{600 \mu m}{80 \mu m} \times 875 \mu s \sim 6.5 \text{ ms}$. The same equations employed to calculate the intermixing coefficient of Ni and Fe in SS316L/IN718 bimetallic structure were utilized here as well. The intermixing of the primary solvents Ni and Fe was observed for a diffusion zone of

approximately 600 μm and the intermixing coefficient of Ni and Fe was estimated to be $4.46 \times 10^{-5} \text{ m}^2/\text{s}$ and $4.22 \times 10^{-5} \text{ m}^2/\text{s}$, respectively, based on a time of 6.5 ms. Figure 24, however, presents the intermixing coefficient of Ni and Fe as a function of time.

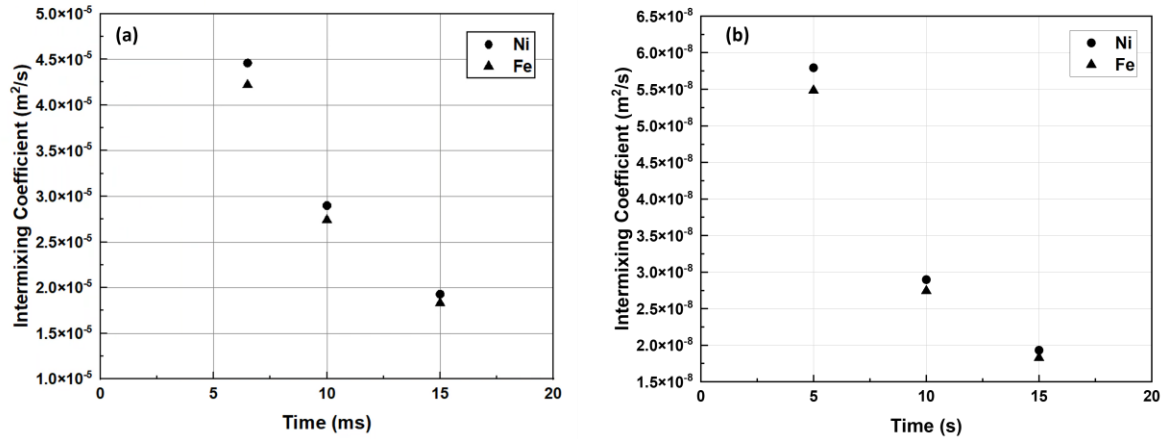


Figure 24: Intermixing coefficient of Ni and Fe as a function of time in SS316L/IN625 bimetallic structures: (a) Time in ms. (b) Time in s

The mechanical properties of the SS316L/IN625 bimetallic structure derived from instrumented nanoindentation are presented in Figure 23(b). In general, IN625 has higher hardness than SS316L, while the interface region was observed to have hardness in between the IN625 and SS316L structure. Typically, the nanohardness of additively manufactured SS316L ranges from $3.4 \pm 0.69 \text{ GPa}$ to $3.7 \pm 0.64 \text{ GPa}$ [83]. Tripathy et al. [84] reported the room temperature nanohardness of additively manufactured IN625 to be around 4.85 GPa. Tong et al. [85] reported the fabrication of gradient SS316L/IN625 joint and investigated the phase composition and microstructure using LENS technology (OPTOMECH LENS 150 printer equipped with a 400 W IPG laser and a two-nozzle coaxial powder feed system). The reported yield strength and UTS were 486 MPa and 672 MPa, respectively for the SS316L/IN625 gradient joint.

CHAPTER 5: SUMMARY

Bimetallic structures via LPBF have been investigated and the findings are:

1. Fully dense and crack-free fabrication of SS316L/IN718 bimetallic structures was achieved. The presence of negligible pores and nanohardness across the interface region between IN718 and SS316L indicates sound metallurgical bonding between the two alloys. The cross-sectional microstructure near the interface of the bimetallic structure consisted of a typical cellular/columnar structure. In addition, nanoscale Laves, and carbides were also observed. The intermixing of primary solvents (Ni and Fe) was observed for an intermixing zone of approximately 800 μm , and their intermixing coefficient was estimated to be in the order of $10^{-5} \text{ m}^2/\text{s}$ based on time of 10 ms.
2. A maximum temperature of approximately 3400 K was predicted in the LPBF of SS316L/IN718 bimetallic structures via the SS316L vs IN718 diffusion couple study. The self-diffusion coefficient of Ni was estimated to be $1.45 \times 10^{-8} \text{ m}^2/\text{s}$ at 3400 K which was extrapolated from the self-diffusion coefficients of Ni data (without the influence of convection) by Meyer et al. The intermixing coefficient of Ni estimated in SS316L/IN718 bimetallic structure was observed to be $6.5 \times 10^{-5} \text{ m}^2/\text{s}$ based on time of 10 ms. Thus, a difference in 3 orders of magnitude indicates a potential role of convection in addition to diffusion in the LPBF process.
3. Based on the extrapolated self-diffusion coefficient of Ni ($1.45 \times 10^{-8} \text{ m}^2/\text{s}$) at 3400 K, the period (time) during which the intermixing zone in SS316L/IN718 bimetallic structure fabricated via LPBF basically went through a heat treatment (i.e., annealing) was estimated, and it was observed to be approximately 6.51 s

4. The interface region of SS316L/IN718 bimetallic structure annealed at 850 °C for 120h exhibited the highest nanohardness of 4.54 ± 0.49 GPa while the interface region of SS316L/IN718 bimetallic structure annealed at 1050 °C for 24h showed the lowest nanohardness of 3.29 ± 0.32 GPa. The intermixing zone of the annealed SS316L/IN718 bimetallic structures were observed to increase with the increase in temperatures, however, as-fabricated SS316L/IN718 bimetallic structures showed the maximum intermixing zone of approximately 800 μm . Further investigation is warranted to understand the variation in diffusion zone between the as-fabricated and annealed bimetallic structures.
5. The investigation of SS316L/IN625 bimetallic structures also revealed nearly dense and crack-free fabrication via LPBF. The presence of negligible pores and nanohardness across the interface region between IN625 and SS316L indicates sound metallurgical bonding between the two alloys. In addition to the Laves phase, the cross-sectional microstructure near the interface of the bimetallic structure consisted of a typical cellular/columnar structure. The intermixing of primary solvents (Ni and Fe) was observed for a distance of approximately 600 μm , and their intermixing coefficient was estimated to be in the order of 10^{-5} m^2/s based on time of 6.5 ms.

APPENDIX: PUBLICATIONS AND CONFERENCES

List of Publications

1. **Mahmud, A.**; Ayers, N.; Huynh, T.; Sohn, Y. Additive Manufacturing of SS316L/IN718 Bimetallic Structure via Laser Powder Bed Fusion. *Materials*, 2023.
<https://doi.org/10.3390/ma16196527>
2. A. Mehta, T. Huynh, N. Kljestan, K. Graydon, **A. Mahmud**, M. Knezevic, B. McWilliams, K. Cho, Y. Sohn, Additive Manufacturing of $Al_{18}Co_{30}Cr_{10}Fe_{10}Ni_{32}$ High Entropy Alloy by Gas Atomization and Laser Powder Bed Fusion, *Materials Letters*, 2023.
<https://doi.org/10.1016/j.matlet.2023.134942>
3. **Mahmud, A.**; Huynh, T.; Zhou, L.; Hyer, H.; Mehta, A.; Imholte, DD.; Woolstenhulme, NE.; Wachs, DM.; Sohn, Y. Mechanical Behavior Assessment of Ti-6Al-4V ELI Alloy Produced by Laser Powder Bed Fusion. *Metals*, 2021.
<https://doi.org/10.3390/met11111671>

List of Conferences

1. **A. Mahmud**, Y. Sohn, “Compositional Redistribution, Phase Transformation, Microstructural Development in SS316L/IN625 Bimetallic Structures Fabricated by LPBF” A poster presentation at US-Korea Conference (UKC 2023), August 2-5, 2023, Hyatt Regency DFW, Dallas, Texas, USA.
2. **A. Mahmud**, N. Ayers, T. Huynh, K. Graydon, Y. Sohn, “Compositional Redistribution, Phase Transformation, Microstructural Development in SS316L/IN718 Bimetallic Structures Fabricated by LPBF” Presented a 20 mins oral presentation at TMS 2023 Annual Meeting & Exhibition, March 19-23, 2023, San Diego, CA, USA.
3. **A. Mahmud**, J. Woo, H. Hyer, J. Kim, T. Huynh, Ab. Mehta, K. Lee, Y. Sohn, “Variation in density, phase constituents, microstructure, surface roughness and modulus/hardness observed from LPBF parametric study of Ti – 6 wt.% Al – 4 wt.% V alloy,” Presented a 15 mins oral presentation at TMS 2022 Annual Meeting & Exhibition, February 27-March 3, 2022, Anaheim, CA, USA.
4. **A. Mahmud**, T. Huynh, L. Zhou, D. Imholte, N. Woolstenhulme, D. Wachs, Y. Sohn, “Mechanical properties, fracture surface and microstructure of additively manufactured Ti6Al4V,” Presented a 15 mins oral presentation at Materials Science & Technology (MS&T20) Virtual, November 2-6, 2020.

LIST OF REFERENCES

- [1] W.E. Frazier, Metal additive manufacturing: A review, *J Mater Eng Perform.* 23 (2014) 1917–1928. <https://doi.org/10.1007/s11665-014-0958-z>.
- [2] T. DebRoy, H.L. Wei, J.S. Zuback, T. Mukherjee, J.W. Elmer, J.O. Milewski, A.M. Beese, A. Wilson-Heid, A. De, W. Zhang, Additive manufacturing of metallic components – Process, structure and properties, *Prog Mater Sci.* 92 (2018) 112–224. <https://doi.org/10.1016/j.pmatsci.2017.10.001>.
- [3] L. Zhou, A. Mehta, B. McWilliams, K. Cho, Y. Sohn, Microstructure, precipitates and mechanical properties of powder bed fused inconel 718 before and after heat treatment, *J Mater Sci Technol.* 35 (2019) 1153–1164. <https://doi.org/10.1016/j.jmst.2018.12.006>.
- [4] D. Herzog, V. Seyda, E. Wycisk, C. Emmelmann, Additive manufacturing of metals, *Acta Mater.* 117 (2016) 371–392. <https://doi.org/10.1016/j.actamat.2016.07.019>.
- [5] C.Y. Yap, C.K. Chua, Z.L. Dong, Z.H. Liu, D.Q. Zhang, L.E. Loh, S.L. Sing, Review of selective laser melting: Materials and applications, *Appl Phys Rev.* 2 (2015). <https://doi.org/10.1063/1.4935926>.
- [6] W.E. King, A.T. Anderson, R.M. Ferencz, N.E. Hodge, C. Kamath, S.A. Khairallah, A.M. Rubenchik, Laser powder bed fusion additive manufacturing of metals; physics, computational, and materials challenges, *Appl Phys Rev.* 2 (2015). <https://doi.org/10.1063/1.4937809>.
- [7] A. Mahmud, T. Huynh, L. Zhou, H. Hyer, A. Mehta, D.D. Imholte, N.E. Woolstenhulme, D.M. Wachs, Y. Sohn, Mechanical behavior assessment of ti-6al-4v eli alloy produced by laser powder bed fusion, *Metals (Basel).* 11 (2021). <https://doi.org/10.3390/met11111671>.

- [8] H. Joo, J. Woo, Y. Sohn, K.-A. Lee, Effect of Process Stopping and Restarting on the Microstructure and Local Property of 316L Stainless Steel Manufactured by Selective Laser Melting Process, *Journal of Korean Powder Metallurgy Institute*. 29 (2022) 1–7. <https://doi.org/10.4150/KPMI.2022.29.1.1>.
- [9] A. Hinojos, J. Mireles, A. Reichardt, P. Frigola, P. Hosemann, L.E. Murr, R.B. Wicker, Joining of Inconel 718 and 316 Stainless Steel using electron beam melting additive manufacturing technology, *Mater Des.* 94 (2016) 17–27. <https://doi.org/10.1016/j.matdes.2016.01.041>.
- [10] B.E. Carroll, R.A. Otis, J.P. Borgonia, J.O. Suh, R.P. Dillon, A.A. Shapiro, D.C. Hofmann, Z.K. Liu, A.M. Beese, Functionally graded material of 304L stainless steel and inconel 625 fabricated by directed energy deposition: Characterization and thermodynamic modeling, *Acta Mater.* 108 (2016) 46–54. <https://doi.org/10.1016/j.actamat.2016.02.019>.
- [11] A. Bandyopadhyay, Y. Zhang, B. Onuiké, Additive manufacturing of bimetallic structures, *Virtual Phys Prototyp.* 17 (2022) 256–294. <https://doi.org/10.1080/17452759.2022.2040738>.
- [12] X. Tian, Z. Zhao, H. Wang, X. Liu, X. Song, Progresses on the additive manufacturing of functionally graded metallic materials, *J Alloys Compd.* 960 (2023). <https://doi.org/10.1016/j.jallcom.2023.170687>.
- [13] S.P. Singh, A. Aggarwal, R.K. Upadhyay, A. Kumar, Processing of IN718-SS316L bimetallic-structure using laser powder bed fusion technique, *Materials and Manufacturing Processes*. 36 (2021) 1028–1039. <https://doi.org/10.1080/10426914.2021.1885701>.
- [14] N. Chen, H.A. Khan, Z. Wan, J. Lippert, H. Sun, S.L. Shang, Z.K. Liu, J. Li, Microstructural characteristics and crack formation in additively manufactured bimetal material of 316L

- stainless steel and Inconel 625, *Addit Manuf.* 32 (2020).
<https://doi.org/10.1016/j.addma.2020.101037>.
- [15] A. Mehta, T. Huynh, N. Kljestan, K. Graydon, A. Mahmud, M. Knezevic, B. McWilliams, K. Cho, Y. Sohn, Additive manufacturing of Al18Co30Cr10Fe10Ni32 high entropy alloy by gas atomization and laser powder bed fusion, *Mater Lett.* 350 (2023).
<https://doi.org/10.1016/j.matlet.2023.134942>.
- [16] N.D. Vallejo, C. Lucas, N. Ayers, K. Graydon, H. Hyer, Y. Sohn, Process optimization and microstructure analysis to understand laser powder bed fusion of 316l stainless steel, *Metals (Basel)*. 11 (2021). <https://doi.org/10.3390/met11050832>.
- [17] A.M. Beese, B.E. Carroll, Review of Mechanical Properties of Ti-6Al-4V Made by Laser-Based Additive Manufacturing Using Powder Feedstock, *JOM*. 68 (2016) 724–734.
<https://doi.org/10.1007/s11837-015-1759-z>.
- [18] H. Hyer, L. Zhou, G. Benson, B. McWilliams, K. Cho, Y. Sohn, Additive manufacturing of dense WE43 Mg alloy by laser powder bed fusion, *Addit Manuf.* 33 (2020).
<https://doi.org/10.1016/j.addma.2020.101123>.
- [19] H. Hyer, L. Zhou, S. Park, G. Gottsfriz, G. Benson, B. Tolentino, B. McWilliams, K. Cho, Y. Sohn, Understanding the Laser Powder Bed Fusion of AlSi10Mg Alloy, *Metallography, Microstructure, and Analysis*. 9 (2020) 484–502. <https://doi.org/10.1007/s13632-020-00659-w>.
- [20] L. Zhou, T. Huynh, S. Park, H. Hyer, A. Mehta, S. Song, Y. Bai, B. McWilliams, K. Cho, Y. Sohn, Laser powder bed fusion of Al–10 wt% Ce alloys: microstructure and tensile property, *J Mater Sci*. 55 (2020) 14611–14625. <https://doi.org/10.1007/s10853-020-05037-z>.

- [21] T. Huynh, A. Mehta, K. Graydon, J. Woo, S. Park, H. Hyer, L. Zhou, D.D. Imholte, N.E. Woolstenhulme, D.M. Wachs, Y. Sohn, Microstructural Development in Inconel 718 Nickel-Based Superalloy Additively Manufactured by Laser Powder Bed Fusion, *Metallography, Microstructure, and Analysis*. 11 (2022) 88–107. <https://doi.org/10.1007/s13632-021-00811-0>.
- [22] A. Mehta, L. Zhou, T. Huynh, S. Park, H. Hyer, S. Song, Y. Bai, D. Devin Imholte, N.E. Woolstenhulme, D.M. Wachs, Y. Sohn, F. UCF Pegasus Professor, L.-M. Professor of Engineering, Additive Manufacturing and Mechanical properties of the dense and crack free Zr-modified Aluminum Alloy 6061 fabricated by the Laser-Powder Bed Fusion, 2021.
- [23] Y. Zhong, L.E. Rännar, L. Liu, A. Koptuyg, S. Wikman, J. Olsen, D. Cui, Z. Shen, Additive manufacturing of 316L stainless steel by electron beam melting for nuclear fusion applications, *Journal of Nuclear Materials*. 486 (2017) 234–245. <https://doi.org/10.1016/j.jnucmat.2016.12.042>.
- [24] N.S. Al-Mamun, K. Mairaj Deen, W. Haider, E. Asselin, I. Shabib, Corrosion behavior and biocompatibility of additively manufactured 316L stainless steel in a physiological environment: the effect of citrate ions, *Addit Manuf.* 34 (2020). <https://doi.org/10.1016/j.addma.2020.101237>.
- [25] D. Kong, X. Ni, C. Dong, L. Zhang, C. Man, J. Yao, K. Xiao, X. Li, Heat treatment effect on the microstructure and corrosion behavior of 316L stainless steel fabricated by selective laser melting for proton exchange membrane fuel cells, *Electrochim Acta*. 276 (2018) 293–303. <https://doi.org/10.1016/j.electacta.2018.04.188>.

- [26] P. Dhaiweegan, N. Elangovan, T. Nishimura, N. Rajendran, Corrosion behavior of 316L and 304 stainless steels exposed to industrial-marine-urban environment: Field study, *RSC Adv.* 6 (2016) 47314–47324. <https://doi.org/10.1039/c6ra04015b>.
- [27] F. Caiazzo, V. Alfieri, G. Corrado, P. Argenio, Laser powder-bed fusion of Inconel 718 to manufacture turbine blades, *International Journal of Advanced Manufacturing Technology.* 93 (2017) 4023–4031. <https://doi.org/10.1007/s00170-017-0839-3>.
- [28] R. Ghanavati, H. Naffakh-Moosavy, M. Moradi, Additive manufacturing of thin-walled SS316L-IN718 functionally graded materials by direct laser metal deposition, *Journal of Materials Research and Technology.* 15 (2021) 2673–2685. <https://doi.org/10.1016/j.jmrt.2021.09.061>.
- [29] P. Mohammadpour, H. Yuan, A.B. Phillion, Microstructure evolution of Inconel 625 alloy during single-track Laser Powder Bed Fusion, *Addit Manuf.* 55 (2022). <https://doi.org/10.1016/j.addma.2022.102824>.
- [30] V. Shankar, K. Bhanu, S. Rao, S.L. Mannan, Microstructure and mechanical properties of Inconel 625 superalloy, n.d. www.elsevier.nl/locate/jnucmat.
- [31] M.R. Stoudt, E.A. Lass, D.S. Ng, M.E. Williams, F. Zhang, C.E. Campbell, G. Lindwall, L.E. Levine, The Influence of Annealing Temperature and Time on the Formation of δ -Phase in Additively-Manufactured Inconel 625, *Metall Mater Trans A Phys Metall Mater Sci.* 49 (2018) 3028–3037. <https://doi.org/10.1007/s11661-018-4643-y>.
- [32] E.A. Lass, M.R. Stoudt, M.E. Williams, M.B. Katz, L.E. Levine, T.Q. Phan, T.H. Gnaeupel-Herold, D.S. Ng, Formation of the Ni₃Nb δ -Phase in Stress-Relieved Inconel 625 Produced via Laser Powder-Bed Fusion Additive Manufacturing, *Metall Mater Trans A Phys Metall Mater Sci.* 48 (2017) 5547–5558. <https://doi.org/10.1007/s11661-017-4304-6>.

- [33] SLM Solutions, Materials Data Sheet, SS316L, 2023.
- [34] SLM Solutions, Materials Data Sheet, IN718, 2023.
- [35] SLM Solutions, Materials Data Sheet, IN625, 2023.
- [36] R. Ghanavati, H. Naffakh-Moosavy, Additive manufacturing of functionally graded metallic materials: A review of experimental and numerical studies, *Journal of Materials Research and Technology*. 13 (2021) 1628–1664. <https://doi.org/10.1016/j.jmrt.2021.05.022>.
- [37] I.E. Locci, C.L. Bowman, T.P. Gabbs, Development of High Temperature Dissimilar Joint Technology for Fission Surface Power Systems, in: 4th International Brazing and Soldering Conference, 2009.
- [38] R. Ghanavati, E. Lannunziata, E. Norouzi, S. Bagherifard, L. Iuliano, A. Saboori, Design and development of SS316L-IN718 functionally graded materials via laser powder bed fusion, *Mater Lett*. 349 (2023) 134793. <https://doi.org/10.1016/j.matlet.2023.134793>.
- [39] X. Mei, X. Wang, Y. Peng, H. Gu, G. Zhong, S. Yang, Interfacial characterization and mechanical properties of 316L stainless steel/inconel 718 manufactured by selective laser melting, *Materials Science and Engineering A*. 758 (2019) 185–191. <https://doi.org/10.1016/j.msea.2019.05.011>.
- [40] Y.S. Kim, D. Yun, J.H. Han, M.R.U. Ahsan, E.W. Huang, J. Jain, C. Ji, D.B. Kim, S.Y. Lee, Bimetallic additively manufactured structure (BAMS) of Inconel 625 and austenitic stainless steel: effect of heat-treatment on microstructure and mechanical properties, *International Journal of Advanced Manufacturing Technology*. 121 (2022) 7539–7549. <https://doi.org/10.1007/s00170-022-09723-x>.

- [41] D.R. Feenstra, A. Molotnikov, N. Birbilis, Effect of energy density on the interface evolution of stainless steel 316L deposited upon IN625 via directed energy deposition, *J Mater Sci.* 55 (2020) 13314–13328. <https://doi.org/10.1007/s10853-020-04913-y>.
- [42] M.R.U. Ahsan, X. Fan, G.J. Seo, C. Ji, M. Noakes, A. Nycz, P.K. Liaw, D.B. Kim, Microstructures and mechanical behavior of the bimetallic additively-manufactured structure (BAMS) of austenitic stainless steel and Inconel 625, *J Mater Sci Technol.* 74 (2021) 176–188. <https://doi.org/10.1016/j.jmst.2020.10.001>.
- [43] M.R.U. Ahsan, A.N.M. Tanvir, G.J. Seo, B. Bates, W. Hawkins, C. Lee, P.K. Liaw, M. Noakes, A. Nycz, D.B. Kim, Heat-treatment effects on a bimetallic additively-manufactured structure (BAMS) of the low-carbon steel and austenitic-stainless steel, *Addit Manuf.* 32 (2020). <https://doi.org/10.1016/j.addma.2020.101036>.
- [44] C. Narayan, J.I. Goldstein, Low temperature diffusivity measurements in the FeNi system using STEM techniques, *Metallurgical and Materials Transactions A.* 14 (1983) 2737–2439.
- [45] D.C. Dean, J.I. Goldstein, Determination of the Interdiffusion Coefficients in the Fe-Ni and Fe-Ni-P Systems below 900 ~, *Metallurgical Transactions A.* 17 (1986) 1131–1138.
- [46] T. Ustad, H. Sorum, Interdiffusion in the Fe-Ni, Ni-Co, and Fe-Co Systems, *Phys. Stat. Sol.* (a). 20 (1973).
- [47] R. Arifin, Y. Winardi, Y.A. Wicaksono, L. Poriwikawa, Darminto, A. Selamat, W.T. Putra, M. Malyadi, Atomic diffusion at the Ni–Ti liquid interface using molecular dynamics simulations, *Canadian Metallurgical Quarterly.* 61 (2022) 359–365. <https://doi.org/10.1080/00084433.2022.2039869>.

- [48] A. V. Yakubovich, A. V. Verkhovtsev, M. Hanauske, A. V. Solov'Yov, Computer simulation of diffusion process at interfaces of nickel and titanium crystals, *Comput Mater Sci.* 76 (2013) 60–64. <https://doi.org/10.1016/j.commatsci.2012.12.039>.
- [49] M. Walbrühl, A. Blomqvist, P.A. Korzhavyi, Atomic diffusion in liquid nickel: First-principles modeling, *Journal of Chemical Physics.* 148 (2018). <https://doi.org/10.1063/1.5026348>.
- [50] A. Meyer, S. Stüber, D. Holland-Moritz, O. Heinen, T. Unruh, Determination of self-diffusion coefficients by quasielastic neutron scattering measurements of levitated Ni droplets, *Phys Rev B.* 77 (2008). <https://doi.org/10.1103/physrevb.77.092201>.
- [51] J.P. Leonard, T.J. Renk, M.O. Thompson, M.J. Aziz, Solute Diffusion in Liquid Nickel Measured by Pulsed Ion Beam Melting, n.d.
- [52] S.M. Chathoth, A. Meyer, M.M. Koza, F. Juranyi, Atomic diffusion in liquid Ni, NiP, PdNiP, and PdNiCuP alloys, *Appl Phys Lett.* 85 (2004) 4881–4883. <https://doi.org/10.1063/1.1825617>.
- [53] H. Hyer, L. Zhou, S. Park, G. Gottsfriz, G. Benson, B. Tolentino, B. McWilliams, K. Cho, Y. Sohn, Understanding the Laser Powder Bed Fusion of AlSi10Mg Alloy, *Metallography, Microstructure, and Analysis.* 9 (2020) 484–502. <https://doi.org/10.1007/s13632-020-00659-w>.
- [54] A. Mahmud, N. Ayers, T. Huynh, Y. Sohn, Additive Manufacturing of SS316L/IN718 Bimetallic Structure via Laser Powder Bed Fusion, *Materials.* 16 (2023) 6527. <https://doi.org/10.3390/ma16196527>.

- [55] E. Perez, T. Patterson, Y. Sohn, Interdiffusion analysis for NiAl versus superalloys diffusion couples, in: *J Phase Equilibria Diffus*, 2006: pp. 659–664. <https://doi.org/10.1361/154770306X153701>.
- [56] C.C. Kammerer, S. Behdad, L. Zhou, F. Betancor, M. Gonzalez, B. Boesl, Y.H. Sohn, Diffusion kinetics, mechanical properties, and crystallographic characterization of intermetallic compounds in the Mg-Zn binary system, *Intermetallics (Barking)*. 67 (2015) 145–155. <https://doi.org/10.1016/j.intermet.2015.08.001>.
- [57] Y. Park, D.D. Keiser, Y.H. Sohn, Interdiffusion and reactions between U-Mo and Zr at 650°C as a function of time, *Journal of Nuclear Materials*. 456 (2015) 351–358. <https://doi.org/10.1016/j.jnucmat.2014.09.040>.
- [58] Y. Park, K. Huang, A. Paz y Puente, H.S. LEE, B.H. Sencer, J.R. Kennedy, Y.H. Sohn, Diffusional Interaction Between U-10 wt pct Zr and Fe at 903 K, 923 K, and 953 K (630 °C, 650 °C, and 680 °C), *Metall Mater Trans A Phys Metall Mater Sci*. 46 (2015) 72–82. <https://doi.org/10.1007/s11661-014-2277-2>.
- [59] L. Zhou, C. Kammerer, A. Giri, K. Cho, Y. Sohn, Microstructural Development and Ternary Interdiffusion in Ni-Mn-Ga Alloys, *Metall Mater Trans A Phys Metall Mater Sci*. 46 (2015) 5572–5587. <https://doi.org/10.1007/s11661-015-3123-x>.
- [60] L. Zhou, A. Mehta, K. Cho, Y. Sohn, Composition-dependent interdiffusion coefficient, reduced elastic modulus and hardness in γ -, γ' - and β -phases in the Ni-Al system, *J Alloys Compd*. 727 (2017) 153–162. <https://doi.org/10.1016/j.jallcom.2017.07.256>.
- [61] C. Eduardo Pinedo, A. Paulo Tschiptschin, R. Esc, Low temperature plasma carburizing of AISI 316L austenitic stainless steel and AISI F51 duplex stainless steel, 2013.

- [62] W. Woo, J.S. Jeong, D.K. Kim, C.M. Lee, S.H. Choi, J.Y. Suh, S.Y. Lee, S. Harjo, T. Kawasaki, Stacking Fault Energy Analyses of Additively Manufactured Stainless Steel 316L and CrCoNi Medium Entropy Alloy Using In Situ Neutron Diffraction, *Sci Rep.* 10 (2020). <https://doi.org/10.1038/s41598-020-58273-3>.
- [63] S. Mahadevan, S. Nalawade, J.B. Singh, A. Verma, B. Paul, K. Ramaswamy, Evolution of Delta Phase Microstructure in Alloy 718, 2010.
- [64] S. Mohd Yusuf, N. Mazlan, N.H. Musa, X. Zhao, Y. Chen, S. Yang, N.A. Nordin, S.A. Mazlan, N. Gao, Microstructures and Hardening Mechanisms of a 316L Stainless Steel/Inconel 718 Interface Additively Manufactured by Multi-Material Selective Laser Melting, *Metals (Basel)*. 13 (2023). <https://doi.org/10.3390/met13020400>.
- [65] W.M. Tucho, P. Cuvillier, A. Sjolyst-Kverneland, V. Hansen, Microstructure and hardness studies of Inconel 718 manufactured by selective laser melting before and after solution heat treatment, *Materials Science and Engineering: A*. 689 (2017) 220–232. <https://doi.org/10.1016/j.msea.2017.02.062>.
- [66] D. Zhang, W. Niu, X. Cao, Z. Liu, Effect of standard heat treatment on the microstructure and mechanical properties of selective laser melting manufactured Inconel 718 superalloy, *Materials Science and Engineering: A*. 644 (2015) 32–40. <https://doi.org/10.1016/j.msea.2015.06.021>.
- [67] L. Boltzmann, Zur Integration der Diffusionsgleichung bei variablen Diffusionscoefficienten, *Ann Phys.* 289 (1894) 959–964. <https://doi.org/10.1002/andp.18942891315>.

- [68] C.C. Kammerer, N.S. Kulkarni, R.J. Warmack, Y.H. Sohn, Interdiffusion and impurity diffusion in polycrystalline Mg solid solution with Al or Zn, *J Alloys Compd.* 617 (2014) 968–974. <https://doi.org/10.1016/j.jallcom.2014.07.193>.
- [69] M. V. Pantawane, Y.H. Ho, S.S. Joshi, N.B. Dahotre, Computational Assessment of Thermokinetics and Associated Microstructural Evolution in Laser Powder Bed Fusion Manufacturing of Ti6Al4V Alloy, *Sci Rep.* 10 (2020). <https://doi.org/10.1038/s41598-020-63281-4>.
- [70] M.A. Dayananda, Y.H. Sohn, Average Effective Interdiffusion Coefficients and Their Applications for Isothermal Multicomponent Diffusion Couples, *Scr Mater.* 35 (1996) 683–688.
- [71] J. England, M.J. Uddin, E. Ramirez-Cedillo, D. Karunarathne, S. Nasrazadani, T.D. Golden, H.R. Siller, Nanoindentation Hardness and Corrosion Studies of Additively Manufactured 316L Stainless Steel, *J Mater Eng Perform.* 31 (2022) 6795–6805. <https://doi.org/10.1007/s11665-02>.
- [72] M.A. Dayananda, An Analysis of Concentration Profiles for Fluxes, Diffusion Depths, and Zero-Flux Planes in Multicomponent Diffusion, n.d.
- [73] M. Elsaß, C. Kontermann, M. Oechsner, Temperature influence on the development of interdiffusion phenomena in MCrAlY-coated nickel-based superalloys, *Materwiss Werksttech.* 52 (2021) 248–260. <https://doi.org/10.1002/mawe.202000270>.
- [74] G.H. Cao, T.Y. Sun, C.H. Wang, X. Li, M. Liu, Z.X. Zhang, P.F. Hu, A.M. Russell, R. Schneider, D. Gerthsen, Z.J. Zhou, C.P. Li, G.F. Chen, Investigations of γ' , γ'' and δ precipitates in heat-treated Inconel 718 alloy fabricated by selective laser melting, *Mater Charact.* 136 (2018) 398–406. <https://doi.org/10.1016/j.matchar.2018.01.006>.

- [75] C. Zhou, S. Hu, Q. Shi, H. Tao, Y. Song, J. Zheng, P. Xu, L. Zhang, Improvement of corrosion resistance of SS316L manufactured by selective laser melting through subcritical annealing, *Corros Sci.* 164 (2020). <https://doi.org/10.1016/j.corsci.2019.108353>.
- [76] C. V. Funch, F.B. Grumsen, A.B. da Silva Fanta, T.L. Christiansen, M.A.J. Somers, Thermal stability of hierarchical microstructural features in additively manufactured stainless steel, *Heliyon.* 9 (2023). <https://doi.org/10.1016/j.heliyon.2023.e16555>.
- [77] D. Deng, R.L. Peng, H. Brodin, J. Moverare, Microstructure and mechanical properties of Inconel 718 produced by selective laser melting: Sample orientation dependence and effects of post heat treatments, *Materials Science and Engineering: A.* 713 (2018) 294–306. <https://doi.org/10.1016/j.msea.2017.12.043>.
- [78] A.A. Kodentsov, G.F. Bastin, F.J.J. Van Loo, The diffusion couple technique in phase diagram determination, 2001. www.elsevier.com/locate/jallcom.
- [79] I. Zhirnov, S. Mekhontsev, B. Lane, S. Grantham, N. Bura, Accurate determination of laser spot position during laser powder bed fusion process thermography, *Manuf Lett.* 23 (2020) 49–52. <https://doi.org/10.1016/j.mfglet.2019.12.002>.
- [80] F. Zhang, L.E. Levine, A.J. Allen, S.W. Young, M.E. Williams, M.R. Stoudt, K.W. Moon, J.C. Heigel, J. Ilavsky, Phase Fraction and Evolution of Additively Manufactured (AM) 15-5 Stainless Steel and Inconel 625 AM-Bench Artifacts, *Integr Mater Manuf Innov.* 8 (2019) 362–377. <https://doi.org/10.1007/s40192-019-00148-1>.
- [81] H. Hyer, R. Newell, D. Matejczyk, S. Hsie, M. Anthony, L. Zhou, C. Kammerer, Y. Sohn, Microstructural Development in As Built and Heat Treated IN625 Component Additively Manufactured by Laser Powder Bed Fusion, *J Phase Equilibria Diffus.* 42 (2021) 14–27. <https://doi.org/10.1007/s11669-020-00855-9>.

- [82] S. Nucci, Microstructural Development of Inconel 625 Nickel-Based Superalloy as Function of Laser Powder Bed Fusion Parameters, 2021. <https://stars.library.ucf.edu/etd2020/538>.
- [83] J. England, M.J. Uddin, E. Ramirez-Cedillo, D. Karunaratne, S. Nasrazadani, T.D. Golden, H.R. Siller, Nanoindentation Hardness and Corrosion Studies of Additively Manufactured 316L Stainless Steel, *J Mater Eng Perform.* 31 (2022) 6795–6805. <https://doi.org/10.1007/s11665-02>.
- [84] M. Tripathy, M. Munther, K. Davami, A. Beheshti, Surface property study of additively manufactured Inconel 625 at room temperature and 510 °C, *Manuf Lett.* 26 (2020) 69–73. <https://doi.org/10.1016/j.mfglet.2020.10.001>.
- [85] X. Tong, C. Lu, Z. Huang, C. Zhang, F. Chen, Microstructures and mechanical properties of crack-free 316L stainless steel and Inconel 625 joint by using Laser Engineered Net Shaping, *Opt Laser Technol.* 155 (2022). <https://doi.org/10.1016/j.optlastec.2022.108357>.